6

DESIGN, FABRICATION, INSTALLATION, AND PERFORMANCE OF THE ACCELERATOR STRUCTURE

R. P. Borghi, A. L. Eldredge, R. H. Helm, A. V. Lisin, G. A. Loew, Editor and R. B. Neal

The purpose of this chapter is to describe the heart of the accelerator, the periodic waveguide structure which is used to accelerate the electrons. As discussed in Chapter 3, the design of the two-mile machine at SLAC is a logical extension of accelerator developments at Stanford University since 1947.[1,2] By the time the SLAC project was authorized in 1961, Stanford workers had reached a high degree of confidence and familiarity with the design and fabrication of disk-loaded waveguides. Although several other types of periodic structures were investigated as discussed later in this chapter, the disk-loaded waveguide was selected as the best overall structure meeting most design and fabrication criteria.

This chapter is divided into four parts. The first is concerned with a discussion of accelerator theory and selection of characteristic parameters. It is followed by a description of the empirical design used to achieve the selected parameters. The third part is a description of fabrication techniques, assembly, and installation. Finally, a summary of performance is given.

6-1 Theory and selection of characteristic parameters

Choice of operating frequency (RBN)

Because almost all the basic accelerator parameters have frequency dependence, it was first essential to compare the advantages and disadvantages of the various frequency bands and to choose an operating frequency. However, it was not possible to make the choice of frequency by purely analytical methods; the final selection required engineering judgment and reference to previous experience.

The laws of frequency dependence of the principal parameters involved in the design of a linac are listed in Table 6-1. To simplify the comparison, this table assumes direct scaling of the modular dimensions of the accelerating structure. For a specific accelerator some compromises must be made which modify Table 6-1 in certain details but do not alter its general implications.

The energy of electrons from a linear accelerator with negligible beam loading is given by

$$V = K(P_T L r_0)^{1/2} \tag{6-1}$$

where P_T is the total input RF power, L is the total length, r_0 is the shunt impedance per unit length, and K is a constant of which the value depends upon the net RF attenuation in each independently fed accelerator section.

Table 6-1 Frequency dependence of principal machine parameters

Parameter	*Frequency dependence*	*Frequency preference*		*Notes*
		High	*Low*	
Shunt impedance per unit length (r)	$f^{1/2}$	X		a
RF loss factor (Q)	$f^{-1/2}$		X	a
Filling time (t_F)	$f^{-3/2}$	X		a, b
Total RF peak power	$f^{-1/2}$	X		a, b, c
RF feed interval (l)	$f^{-3/2}$		X	a, b
No. of RF feeds	$f^{3/2}$		X	a, b, d
RF peak power per feed	f^{-2}	X		a, b, c
RF energy stored in accelerator	f^{-2}	X		a, b, c
Beam loading ($-dV/di$)	$f^{1/2}$		X	a, b, d
Peak beam current at maximum conversion efficiency	$f^{-1/2}$		X	a, b, c, f
Diameter of beam aperture	f^{-1}		X	a
Maximum RF power available from single source	f^{-2}		X	e
Maximum permissible electric field strength	$f^{1/2}$	X		g
Relative frequency and dimensional tolerances	$f^{1/2}$	X		a, b
Absolute wavelength and dimensional tolerances	$f^{-1/2}$		X	a, b
Power dissipation capability of accelerator structure	f^{-1}		X	a, b, d

Notes:
a. For direct scaling of modular dimensions of accelerator structure.
b. For same RF attenuation in accelerator section between feeds.
c. For fixed electron energy and total length.
d. For fixed total length.
e. When limited by cathode emission.
f. When limited by beam loading.
g. Approximate; empirical.

Since r_0 varies as $f^{1/2}$, the RF power required to produce a given final energy in a fixed length is proportional to $f^{-1/2}$. Thus, considerations of power economy indicated that the operating frequency should be as high as possible. Other advantages of the higher frequencies are the reduced filling time, which varies as $f^{-3/2}$, and reduced energy storage, which varies as f^{-2}. A shorter filling time is advantageous since electrons can be accelerated during a larger fraction of the available RF pulse length. The use of the higher frequencies also results in greater maximum field strength (as limited by breakdown) and larger relative frequency and dimensional tolerances.

From Table 6-1 it can be seen that the maximum frequency which can be used is limited by the diameter of the aperture available for the beam and by the reduced, beam current capability. Another factor against the use of very high frequencies is the increased number of power sources and feeds required. The increased cost of additional RF systems, modulators, and controls, and the increased operational difficulties which are encountered tend to offset the advantages arising from decreased power consumption at high frequencies.

An important consideration not taken into account in Table 6-1 was the degree of conservatism involved in the choice of frequency band. Although linear electron accelerators had been constructed and operated at L-, S-, and X-bands, the largest amount of experience was available at S-band. In fact, to this date all accelerators of this type having energies above 100 MeV have operated at S-band.

To illustrate the scaling laws given in Table 6-1 more specifically, design data for a 20-GeV accelerator 10,000 ft long are given in Table 6-2. Three cases are tabulated corresponding to operating at L-, S-, and X-bands. The specific values in Table 6-2 were based on relations and criteria which are developed later in this section. While each item in Table 6-2 need not be discussed individually, it may be worthwhile to emphasize the following points:

1. An important aspect of the design of the two-mile accelerator was the possibility of increasing the beam energy at some future date from its present maximum of 20 GeV to a higher level between 20 and 40 GeV. For reasons of economy and to avoid prolonged machine shutdown, it appeared desirable to make such an energy expansion possible by increasing the RF power rather than the accelerator length. According to Table 6-2, the L-band structure with a fixed length of 10,000 ft could not be expanded above about 38.4 GeV without experiencing breakdown difficulties.
2. The average RF power requirements were in the ratio 4.1/1.0/0.4 for the L-, S-, and X-band machines, respectively.
3. The maximum peak beam currents and beam powers were in the ratios of 1.7/1.0/0.6 for the L-, S-, and X-band machines, respectively.
4. The aperture available for the beam in the X-band machine (0.255 in.) would have been small enough to cause great concern about beam transmission and accelerator alignment.

Table 6-2 Design parameters of 20-GeV accelerator at three frequencies[a]

Parameter	*Frequency* (*L-Band*) *1000 MHz*	(*S-Band*) *3000 MHz*	(*X-Band*) *9000 MHz*
Shunt impedance r (megohms/meter)	31	53	92
RF loss factor (Q)	2.25×10^4	1.3×10^4	0.75×10^4
Filling time t_F (μsec)	4.31	0.83	0.16
Total RF peak power (MW)	9216	5320	3072
RF feed interval (ft)	52	10	1.92
No. of RF feeds	185	960	4988
RF peak power (MW) per feed	50	5.54	0.62
RF energy (J) stored in accelerator	21,348	2372	264
RF energy (J) required for 1.67-μsec electron beam pulse length	55,112	13,300	5,620
Total average RF power (MW) at 360 pulses/sec	19.84	4.80	2.04
Beam loading ($-dV/di$) (GeV/A)	20.5	35.5	61.5
Peak beam current (mA) at maximum conversion efficiency	544.2	314.2	181.4
Minimum diameter (in.) of beam aperture	2.292	0.764	0.255
Maximum RF peak power (MW) from single source[b]	216	24	2.7
Maximum permissible electric field strength[c] (kV/cm)	133	230	398
Maximum expanded beam energy[d] (GeV)	38.4	66.5	115.0
Relative frequency and dimensional tolerances[e]	1.11×10^{-5}	1.93×10^{-5}	3.34×10^{-5}
Absolute frequency and dimensional tolerances[e]	11 kHz 0.11 mils	58 kHz 0.06 mils	301 kHz 0.04 mils
Average power dissipated per unit area of accelerator surface[f] (W/cm^2)	0.59	0.43	0.53
Average temperature difference (°C) across accelerator wall[g]	0.42	0.10	0.04

[a] Assumptions: $2\pi/3$ mode in constant-gradient structure; $\tau = 0.57$ Np (RF attenuation); $L = 10{,}000$ ft (94.8% effective); 10% power loss in waveguides; 10% beam loading; direct scaling of modular dimensions.

[b] Based on 24 MW available at S-band, values for other frequencies based on scaling as f^{-2}.

[c] Based on maximum gradient obtained to date at S-band; values for other frequencies based on scaling as $f^{1/2}$.

[d] As limited by maximum permissible field strength.

[e] For 1% loss in beam energy.

[f] Based on 360 pulses/sec and 1.6-μsec electron beam pulse length.

[g] Based on copper wall 3, 1, and $\frac{1}{4}$ cm thick at L-, S-, and X-bands, respectively.

5. The X-band accelerator ranked highest in terms of maximum expanded energy capability, but the higher energies required X-band sources of higher peak power than were available. For example, operation at 40 GeV would have required 4988 sources each producing 2.5 MW of peak RF power.
6. Expansion of the L-band accelerator to 40 GeV would have required that each of the 185 feed points be supplied with 200 MW of peak power. Such power would have been much higher than the power output obtainable from a single L-band source and would have required parallel operation of several sources at each feed.
7. Expansion of the S-band machine to 40 GeV would have required 22.2 MW at each of the 960 feed points. Power outputs above this level had already been obtained quite easily from single S-band sources.
8. The *relative* frequency and dimensional tolerances favored the use of the higher frequencies. Relative dimensional tolerances are probably more significant than absolute tolerances, since the former are a better measure of the difficulties involved in critical machining operations.
9. The average power dissipated per unit area of accelerator surface was not significantly different in the three designs because the increased wall area at low frequency tended to compensate for the higher power required and vice versa. However, the average temperature difference across the accelerator wall, which is a measure of the degree of detuning of the structure, was highest at L-band and lowest at X-band.

It would have been possible to compare accelerator designs at the various frequencies in further detail. The designs that were chosen for illustrative purposes were based upon direct scaling of the modular dimensions of existing S-band accelerator structures. An improved design at a particular frequency from the standpoint of overall economy or performance may have been obtained by deviating from the scaling laws that were used. For example, the L-band design might have been improved by decreasing the feed interval and using a larger number of sources, and by increasing the RF and beam pulse lengths while decreasing the pulse repetition rate. However, this would not have affected the total peak power requirement or the maximum, field strength capability. Similar alterations might have been made at S- and X-bands to improve certain characteristics of these designs. However, such changes would not have modified appreciably the general conclusion that was reached, namely that S-band was the optimum choice for the two-mile accelerator for reasons implicit in the scaling laws of Table 6-1 and the illustrative examples of Table 6-2.

Product of RF power and accelerator length (RBN)

The energy of electrons from a linear accelerator with negligible beam loading was given by Eq. (6-1). To estimate the power-length product of the two-mile accelerator, the values of two important parameters discussed later in this

chapter are anticipated: the shunt impedance r_0 is assumed to be 53 megohms/meter and $K = 0.82$. The objective was an accelerator capable of producing electrons with an energy of 20 GeV under conditions of 10% beam loading. The no-load energy, therefore, had to be 22.22 GeV. To obtain a realistic estimate, 10% of the RF power was assumed to be dissipated in the RF transmission lines between the power sources and the accelerator, and 5.2% of the accelerator length was assumed to be used for auxiliary in-line devices not contributing to the acceleration process.

Substituting the above assumptions into Eq. (6-1), the required product of total RF power and accelerator length was

$$P_{OT}L = 16.12 \times 10^{14} \text{ W-cm}$$
$$= 5.30 \times 10^{7} \text{ MW-ft}$$

Selection of accelerator length (RBN)

Once the RF power–accelerator length product had been determined, these two quantities had to be chosen individually. The following factors influenced these selections:

MAXIMUM ELECTRIC GRADIENT. As discussed earlier in this chapter, the design objective was a linear electron accelerator initially capable of producing a maximum energy of 20 GeV, with an ultimate capability of 40 GeV energy by addition of RF power without increase of accelerator length. This objective required that the length of the machine be chosen so as to permit the maximum ultimate gradient. The maximum average electric gradient obtained in an operating, S-band, linear accelerator at the time the accelerator was being conceived was approximately 4.5 MeV/ft. Using this figure, a length of approximately 10,000 ft was required to satisfy the ultimate energy objective.

ECONOMIC CONSIDERATIONS. The total cost of an accelerator may be divided into three parts: (a) costs (C_P) which are proportional to the total connected RF power; (b) costs (C_L) which are proportional to the total accelerator length; and (c) fixed costs (C_F) which include research costs and administrative costs, among others.

To be meaningful, these costs had to be based on a time period that included the construction time plus a period judged to represent the useful life of the machine. A period of 10 yr of useful life was used in cost studies. From the fact that RF power and accelerator length have equal weight in the equation for electron energy, it is easy to show that the greatest overall economy results when $C_P = C_L$. Otherwise, the total cost is given by

$$C = \frac{1}{2}\left[\left(\frac{C_P}{C_L}\right)^{1/2} + \left(\frac{C_L}{C_P}\right)^{1/2}\right] C_{(P,L)_{\min}} + C_F \qquad (6\text{-}2)$$

where $C_{(P,L)_{\min}}$ is the minimum value of $C_P + C_L$ (i.e., where $C_P = C_L$).

These cost studies showed that an accelerator length of 10,000 ft was very close to the optimum value to minimize the total project costs over the initially projected 6-yr construction period and a 10-yr period of operation.

LAND AVAILABLITY. There were several potential sites available on Stanford land which seemed suitable for the accelerator project location. An accelerator length of 10,000 ft (plus another 2500 ft, approximately, for research facilities) was possible at most of these sites, but no greater length was available without high land acquisition costs.

Thus the choice of an accelerator length of 10,000 ft satisfied the several conditions discussed above: namely, it permitted operation at the ultimate, expanded energy gradient; it was near optimum from the standpoint of overall economy; and such space was available on Stanford property. Using the power-length product determined in an earlier section led to an initial total connected RF power requirement of

$$P_{OT} = 5.32 \times 10^3 \text{ MW}$$

It should be emphasized that this value of P_{OT} was based upon a particular choice of operating mode ($2\pi/3$) and a particular attenuation parameter ($\tau = 0.57$). Their selection is discussed later in this section. The value of P_{OT} would vary slightly if another mode or another value of τ had been used.

Selection of number of RF power sources and feed interval (RBN)

It was established in the previous section that a total RF peak power of 5320 MW had to be supplied by the power sources in order to achieve an electron energy of 20 GeV with 10% beam loading in a 10,000-ft accelerator. The next logical design decisions were the determination of the number of individual RF power sources and the spacing of the RF feeds along the accelerator length.

In general, it is more economical to obtain a large amount of microwave energy from a small number of high-power sources than from a large number of low-power sources. The basic reason for this fact is that the cost of a power source depends more strongly on the number and kind of operations involved in its fabrication and processing than upon its physical size and output rating. The cost of employment of the power sources in the accelerator system in terms of auxiliary equipment, such as instrumentation, controls, and waveguide equipment, also decreases as the total number of individual sources is reduced. Based upon laboratory and commercial experience with high-power klystron amplifiers, it seemed reasonable to expect that S-band tubes could be constructed to have an average life of 2000 hours or more while producing 24 MW of peak RF power and 22 kW of average RF power. Much higher, peak power levels from single S-band tubes did not appear to be readily obtainable at the time. An electron beam energy of 20 GeV could be obtained by requiring 24 MW of peak output per klystron. For a total RF power of

5320 MW, 240 klystrons producing 24 MW each were needed. For operation at the Stage II level of 40 GeV, 960 tubes producing 24 MW each would be required.

The selection of the feed spacing along the accelerator length will now be discussed. The limiting cases of feed spacing were (a) a single feed for the entire accelerator, and (b) individual feeds for each of the approximately 80,000 individual accelerator cavities. The first extreme was obviously unfeasible because the full RF power could not be transmitted through the accelerator structure. The second extreme would have been prohibitively expensive because of the multiplicity of waveguides and other microwave components and the necessary controls and instrumentation. As described in a later section, there is an optimum, or at least a preferred value, of the net RF attenuation between feed points. The choice of attenuation parameter is a compromise among many factors. The attenuation parameter can be adjusted to the desired value by properly choosing the diameter of the aperture in the disk-loaded structure and the length of the accelerator section—increasing the aperture size increases the group velocity and decreases the attenuation per unit length. Thus a given attenuation parameter can be obtained by either a short accelerator section of high unit attenuation (small aperture), or by a long section of low unit attenuation (large aperture), or by a compromise involving medium length and medium aperture. The main factor in favor of close feed-spacing is that the shunt impedance r_0 of the accelerator structure improves slowly as the group velocity is decreased. This is shown in Fig. 6-1 which applies specifically to the $2\pi/3$ mode, but the same general behavior is true for other modes.

Figure 6-1 Variation of v_g/c and r_0 as a function of cavity number along a 10-ft constant-gradient section.

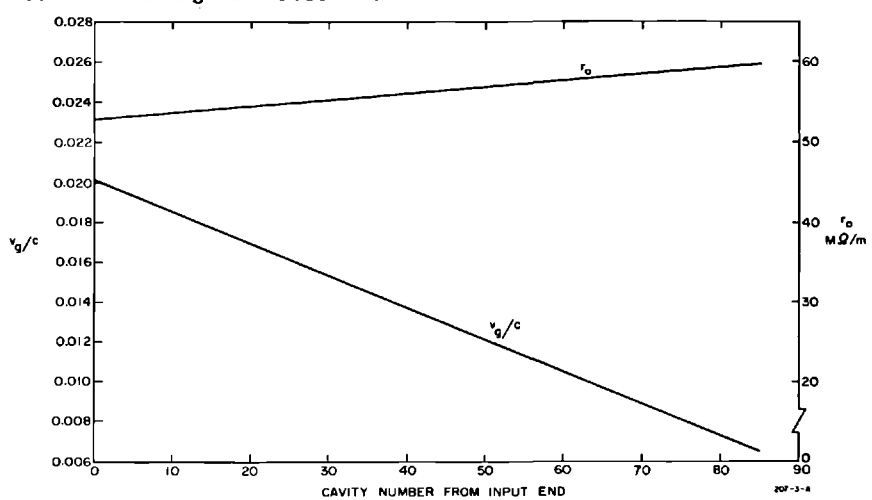

Several considerations limit how closely the feeds should be spaced. These limiting considerations are as follows:

1. Increased costs because of the larger number of components, controls, waveguides, couplers, RF loads, instruments, etc.
2. The complexity of splitting the RF power from each source many times.
3. The decreased aperture available for the electron beam as the group velocity is decreased.
4. Increased operational difficulties because of the increased number of phasing adjustments, monitors, interlocks, etc.

On the basis of these considerations, it was decided that in Stage I, 240 RF power sources supplying 6–24 MW each were to be used, as noted above, and that these sources were to be located at 40-ft intervals along the accelerator length. In Stage II (40 GeV maximum), with 960 RF sources each supplying 6–24 MW, it would not be safe (for reasons of RF breakdown) to feed the combined power outputs of two or more tubes into an accelerator section. Therefore, at least one feed every 40 ft was required in Stage I and at least one feed every 10 ft in Stage II. However, because the shunt impedance would have been reduced by about 15% in going from a 10 to a 40-ft interval, a feed interval of 10 ft was chosen for the two-mile accelerator. This meant that during Stage I operation, with 240 RF power sources, the power output from each klystron had to be divided four ways so as to supply four successive accelerator feeds. The modular arrangement of klystrons, waveguides, and accelerator sections in Stage I was shown in Fig. 5-17. With this arrangement, the number of klystrons could readily be increased to 480, a configuration sometimes called Stage "one and one-half." However, to convert to Stage II operation with 960 RF sources, it will be necessary to double the number of connecting waveguides shown in Fig. 5-17.

Choice of RF pulse length and repetition rate (RBN)

For physics research purposes, it is generally desirable to have the electron beam duty cycle (which is defined as the product of pulse repetition rate and beam pulse length) as high as possible. In fact, as this book is being written, there is a strong incentive toward developing superconducting linacs for which the duty cycle could be as high as 1. In a conventional pulsed linac, the practical upper limit of duty cycle is determined by economic considerations. The RF duty cycle must be greater than the beam duty cycle because a certain time is required to fill the accelerator with RF energy prior to injection of the beam. For the case where the electron beam is injected at a time after the start of the RF pulse equal to one filling time, the ratio of beam-to-RF duty cycles is given by

$$\frac{D_b}{D_{\mathrm{RF}}} = 1 - \frac{t_F}{t_{\mathrm{RF}}} \tag{6-3}$$

where t_F is the accelerator filling time and t_{RF} is the RF pulse length. For example, with $t_F = 0.83$ μsec (the value for $\tau = 0.57$ with the $2\pi/3$ mode) and $t_{RF} = 2.5$ μsec, the maximum duty cycle ratio as given by Eq. (6-3) is 0.67. This may be compared with the value of 0.5 for the original 1-GeV, Stanford Mark III Accelerator. An important point to emphasize is that a given fractional change in RF duty cycle, because of increasing RF pulse length, permits an even larger fractional increase in the beam duty cycle. Thus, increasing the RF pulse length from 2.0 to 2.5 μsec, an increase of 25%, allows a 43% increase in the beam duty cycle (for $t_F = 0.83$ μsec). The factors that place a practical limit on the maximum RF pulse length are the increasing costs of modulator components, such as the pulse transformers and the pulse-forming networks. On the basis of these considerations, the value of 2.5 μsec for the RF pulse length was adopted.

The maximum value of the pulse repetition rate in a linac is governed by three primary factors: (a) The initial cost of power components increases with increasing pulse repetition rate because of their higher average power ratings. (b) It is more difficult and expensive to design and construct high-power modulators at the higher repetition rates. (c) The ac power operational costs for the accelerator power sources increase almost directly with pulse repetition rate.

A maximum repetition rate of 360 pulses/sec was adopted for the two-mile accelerator, in contrast with the maximum rate of 60 pulses/sec for the Stanford Mark III Accelerator. The above combination of higher repetition rate, longer RF pulse length, and shorter filling time yielded a maximum beam duty cycle of about 0.0006, or about ten times greater than that of the Mark III Accelerator.

Selection of operating mode (RBN)

The accelerator structure is a disk-loaded cylindrical waveguide of the form shown in Figs. 5-12 and 5-13, and in Fig. 6-2a, of this chapter.(The alternative configurations in Fig. 6-2c are discussed below.) The efficiency of the structure as an accelerator of electrons is measured by a quantity called the shunt impedance per unit length. This quantity, which has already been introduced earlier and has been designated by the symbol r_0, is defined as the square of the energy gained (in electron volts) by an electron per unit length of accelerator structure for unit RF power dissipation in this same length. Gain in particle energy is used to emphasize that it is not simply the magnitude of the electric field in the accelerator structure which determines the electron energy gain per unit length; rather, it is the amplitude of the Fourier component of the axial field which travels at the electron velocity. The fundamental component is used in most linacs.

The exact value of shunt impedance for a particular configuration of accelerator structure cannot be represented in simple form but can be measured to good accuracy by microwave techniques. An approximate equation

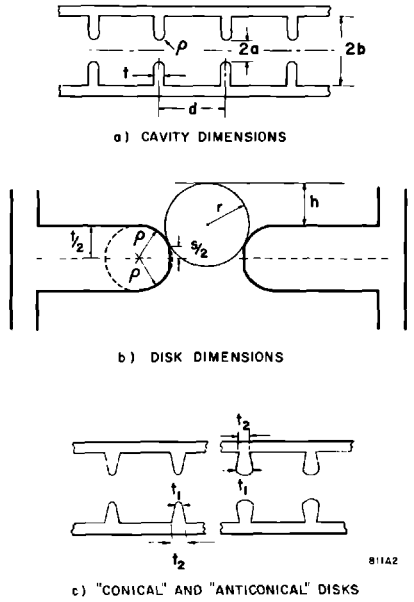

Figure 6-2 Illustration of basic modular dimensions in disk-loaded waveguide structures.

for r_0 which is suitable for studying the effects of varying the cavity dimensions is

$$r_0 = 968\left(\frac{\beta_w}{\delta}\right)\frac{(1-\eta)^2}{n + 2.61\beta_w(1-\eta)}\left(\frac{\sin D/2}{D/2}\right)^2 \tag{6-4}$$

where

β_w is the phase velocity in the structure divided by c,
δ is the skin depth,
t is the disk thickness,
d is the period of the structure,
η is the fraction of the length of the structure which is occupied by disks, i.e., $\eta = t/d = tn/\lambda$
λ is the guide wavelength,
n is λ/d, the number of disks per wavelength, and
D is the transit angle in radians of an electron passing through the cavity gap, i.e., $D = (2\pi/\lambda)(d - t)$

Equation (6-4) can be derived by considering an array of simple "pillbox" cavities. This equation gives too high a value of r_0 for two reasons: (a) the conductivity of the copper walls is never as high as the idealized value used in calculating the numerical constant (968) in the equation; (b) no account

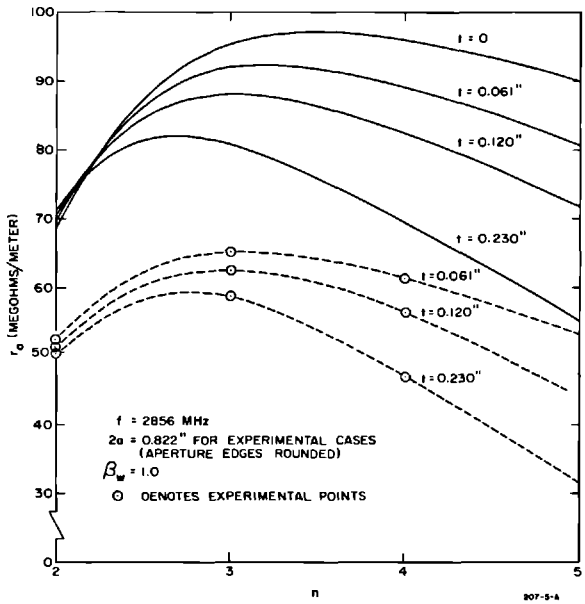

Figure 6-3 Theoretical and experimental curves of shunt impedance (r_0) per unit length versus number of disks per wavelength (n) for various disk thicknesses (t)

is taken of the effect of the disk apertures. Nevertheless, the relative variation of r_0 with the spacing and thickness of the disks given by Eq. (6-4) was confirmed by experimental measurements.

A graph of r_0 versus n for $f = 2856$ MHz based on Eq. (6-4) is shown in Fig. 6-3 for four values of disk thickness, t. Corresponding experimental values obtained from test cavity measurements are also shown. From Fig. 6-3 it is possible to draw some general conclusions. For negligible disk thickness ($t \approx 0$), the optimum number of disks per wavelength is approximately 3.5. As the disk thickness is increased, the optimum value of n decreases. The best value at $t = 0.120$ in. is about $n = 3$. It is about 2.7 for $t = 0.230$ in., which is the chosen disk thickness. The value $n = 3$, corresponding to a phase shift of $2\pi/3$ radians per cavity, was adopted. In addition to the improvement in shunt impedance, the selection of the $2\pi/3$ mode resulted in fewer disks and improved vacuum conductance compared to the $\pi/2$ mode used with the earlier Stanford structures.

The basis for the results described above may be found upon further examination of Eq. (6-4). There are three competing factors: (a) The shunt impedance of the individual cavities is improved by increasing the disk spacing. (b) The fraction of the length available for accelerating fields to act on the electrons is increased as the number of disks per wavelength is

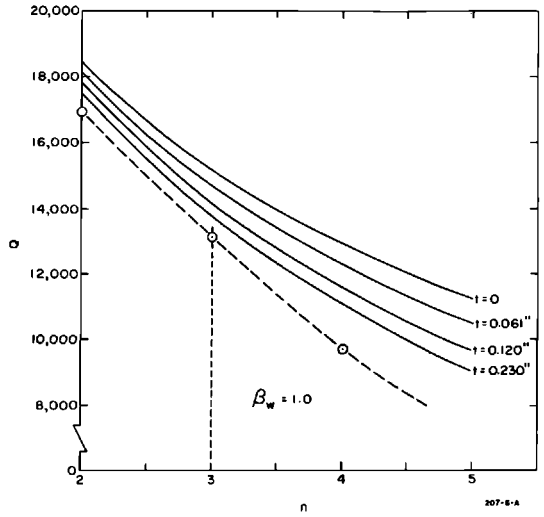

Figure 6-4 Theoretical and experimental curves of Q versus number of disks per wavelength (n) for various disk thicknesses (t).

decreased or as the disk thickness is decreased. (c) As the disk spacing is decreased, the electron transit time is decreased correspondingly, and the average or "effective" field strength acting on the electron is increased as (sin D/2)/(D/2). Thus, considerations (a) and (b) favor small n and small t, whereas consideration (c) favors large n and large t. As t increases, the fractional space occupied by the disks increases so that r_0 peaks at a lower value of n.

An expression similar to Eq. (6-4) may be given for the unloaded quality factor, Q, of an accelerator structure:

$$\frac{Q\delta}{\lambda_0} = \frac{\beta_w(1-\eta)}{n + 2.61\beta_w(1-\eta)} \tag{6-5}$$

where the symbols have the same meaning as given for Eq. (6-4). A plot of Q versus n is given in Fig. 6-4. Some measured values of Q are also shown in the same figure.

The quantity Q was measured in each case by taking two cavity lengths in the ratio of 2:1 in order to cancel out the effect of the end-wall losses as shown in a later section of this chapter. The values of Q are seen to decrease from around 17,000 at $n = 2$ to about 13,000 at $n = 3$ and 10,000 at $n = 4$.

A number of experimental curves for $n = 2$, 3, and 4 are given in Figs. 6-5 and 6-6. The data for these curves were based on disks with unrounded or "square" boundaries. For a given aperture diameter, rounding of the boundary has the effect of increasing the group velocity and decreasing the shunt impedance by about 5 to 10%.

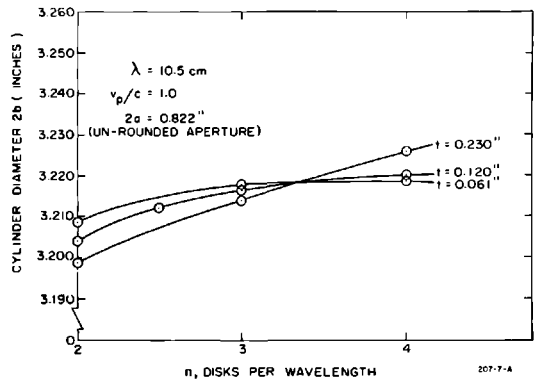

Figure 6-5 Cylinder diameter of disk-loaded waveguide as a function of number of disks per wavelength.

Another observation, which is illustrated in Fig. 6-6, is that the group velocity decreases with increasing disk thickness at a given value of n (except $n = 2$). This indicates that it may be quite misleading to compare the various cases on the basis of the same aperture diameter ($2a$). A better comparison might be made on the basis of the same value of group velocity, which would thereby insure that the filling times for an accelerator section of fixed length were equal in all cases. Alternatively, the comparison might be made on the basis of equal values of the product $v_g Q$, which would give equal values of RF attenuation per unit length in all cases. Adjusting $2a$ to give equal values of v_g would reduce r_0 more severely in the thick disk cases and would thus favor the adoption of thin disks. The limiting factors in reducing disk thickness were the increasing danger of arcing at the disk aperture boundary and the decreasing mechanical strength.

Figure 6-6 Normalized group velocity of disk-loaded waveguide as a function of number of disks per wavelength.

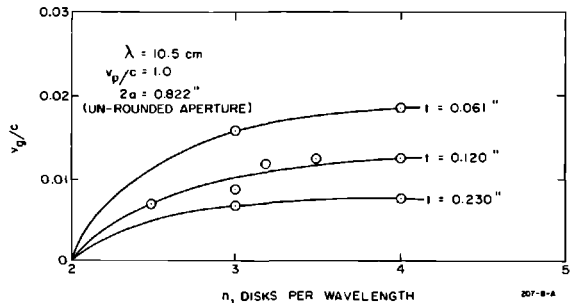

Constant-impedance vs constant-gradient structures (RBN)

When an accelerator of uniform modular dimensions ("constant-impedance" structure) is fed with RF power at one end, there is an exponential decay of power and electric field strength with axial distance from the input end. This means that the average axial electric field is less than the maximum axial field in the structure. On the other hand, it is possible to design a structure of nonuniform modular dimensions in which the axial fields will remain constant over the entire length. Such a structure is referred to as a "constant-gradient structure."

The ratio of maximum-to-average axial electric field strength is unity in the constant-gradient structure, whereas in the constant-impedance structure it is given by

$$\frac{E_0}{V_0/l} = \frac{\tau}{1 - e^{-\tau}} \tag{6-6}$$

where τ is the RF attenuation parameter which can be shown to be equal to $\omega t_F/2Q$. The parameter τ has often been called Il in the literature where I is the RF attenuation in nepers per unit length, and l is the length of the accelerator section. The dependence of τ upon filling time t_F emphasized the importance of comparing the constant-gradient and constant-impedance structures at the same value of τ for each. For equal τ, the two structures have the same filling time, the same stored energies, and the same ratios of input-to-output RF powers.[3] The ratios of maximum-to-average axial electric field strength are shown vs τ in Fig. 6-7. Thus it is clear that the constant-gradient structure

Figure 6-7 Ratios of maximum-to-average axial electric field strengths in constant-impedance and constant-gradient accelerator structures versus τ.

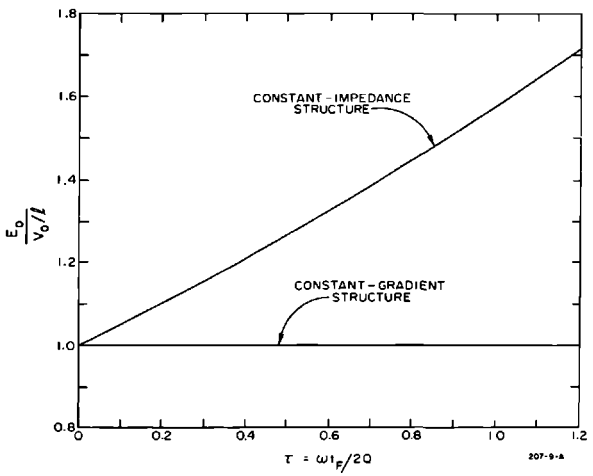

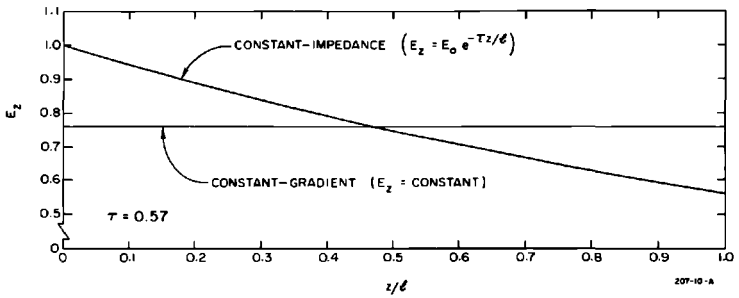

Figure 6-8 Axial field strength versus z/l for equal electron energy gain in constant-gradient and constant-impedance sections.

can produce higher electron energies than an optimized constant-impedance structure when both are operating at the breakdown limit of electric field strength. As indicated in Fig. 6-7, the relative advantage of the constant-gradient accelerator in achieving high gradients without breakdown depends upon the value of τ. Curves of field strength vs axial distance z for the two types of structures are shown in Fig. 6-8 for $\tau = 0.57$.

In addition to the advantage of the reduced ratio of maximum-to-average field strengths, the constant-gradient structure has several other advantages over the constant-impedance structure:

1. The power dissipated per unit length in the constant-gradient accelerator is constant over the entire length of the structure. In contrast, the ratio of power loss at the input end to that at the output end of a constant-impedance structure may be as high as 12.4 to 1. (This magnitude corresponds to a value of the RF attenuation constant $\tau = 1.26$ Np, which gives maximum no-load energy in the constant-impedance accelerator structure.) A plot of the power-loss ratios for the two structures is shown in Fig. 6-9.
2. The constant-gradient structure gives a slightly higher no-load beam energy than the constant-impedance structure and somewhat lower beam-loading derivative $(-dV/di)$. Thus, the constant-gradient structure has greater relative energy advantage in the loaded case than in the unloaded case. The no-load energies for the two structures are shown in Fig. 6-10 and the beam-loading derivatives in Fig. 6-11.
3. The constant-gradient structure has a higher maximum conversion efficiency (ratio of maximum electron beam power to input RF power) and a higher corresponding maximum peak beam current than the constant-impedance structure. Curves of the maximum conversion efficiency, η_{max}, and the corresponding maximum beam current, $i_{\eta_{max}}$, are shown in Fig. 6-12.
4. The constant-gradient accelerator is less frequency-sensitive than the constant-impedance accelerator, as shown in Fig. 6-13.

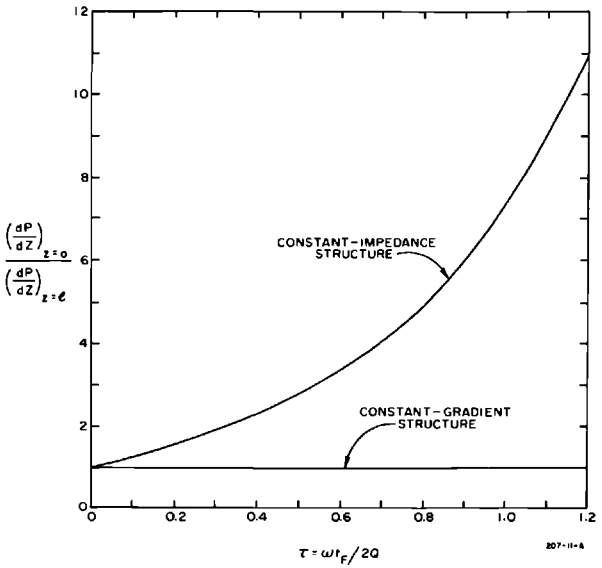

Figure 6-9 Ratio of power losses at input and output ends of accelerator section versus τ for constant-impedance and constant-gradient structures.

Figure 6-10 Unloaded beam energies versus τ for constant-impedance and constant-gradient accelerator structures.

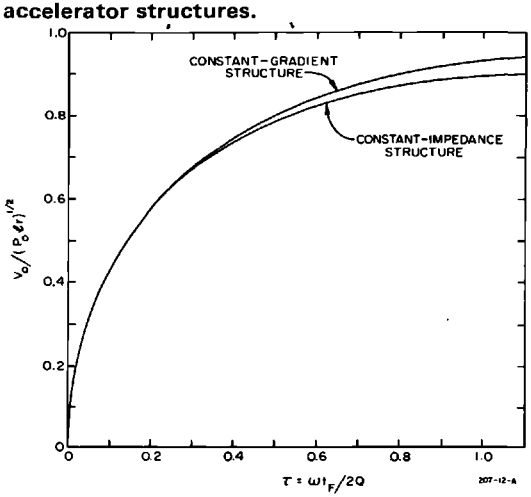

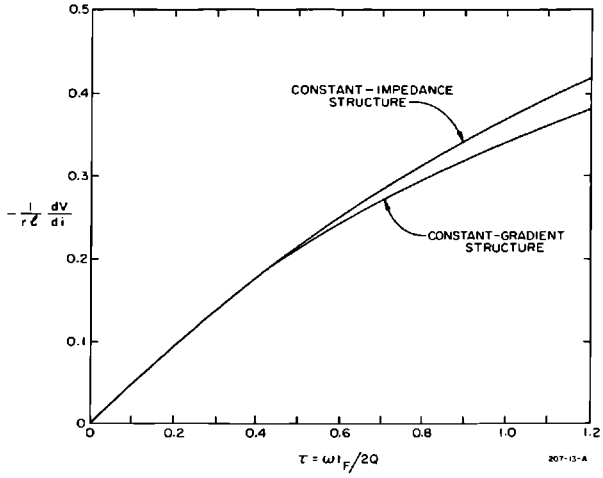

Figure 6-11 Beam loading derivatives versus τ for constant-impedance and constant-gradient accelerator structures.

Figure 6-12 Maximum beam conversion efficiencies and corresponding values of peak beam current versus τ for constant-impedance and constant-gradient accelerator structures.

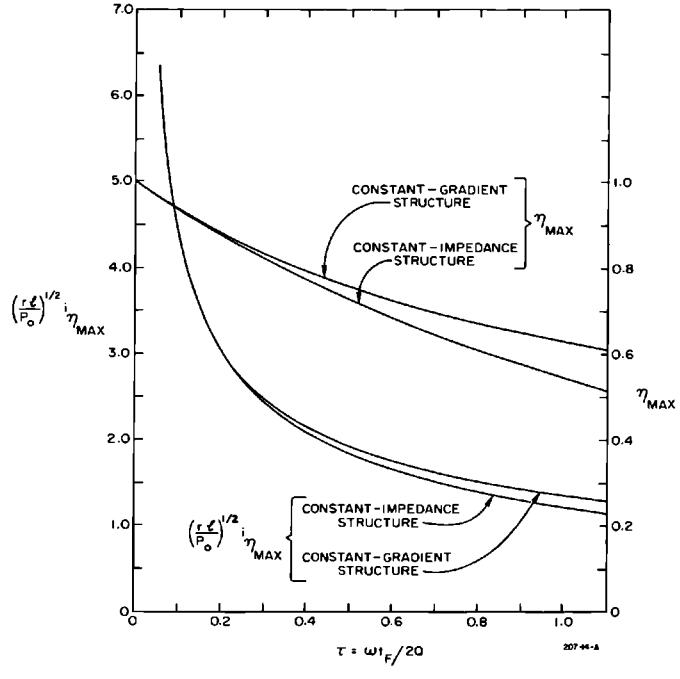

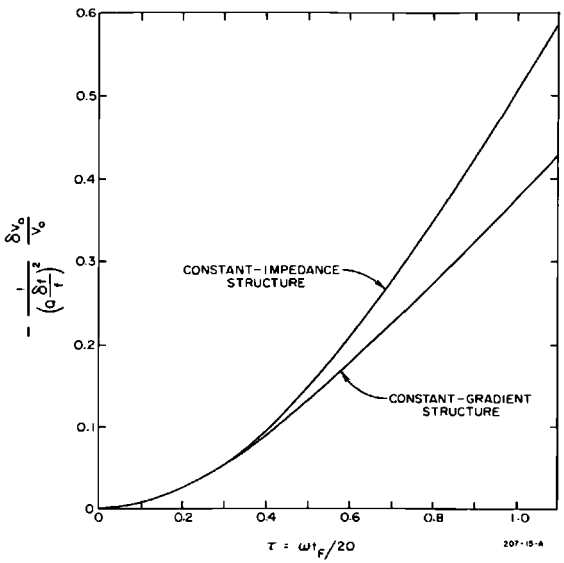

Figure 6-13 Frequency sensitivities versus τ for constant-impedance and constant-gradient accelerator structures.

The factors discussed above depend upon τ, as shown in Figs. 6-7 through 6-13. To illustrate these factors numerically, the characteristics of the two structures are shown in Table 6-3, based upon the parameters of the two-mile accelerator.

5. Amplitude and phase oscillations of the traveling wave caused by the band-pass filter characteristics of the structure may be slightly less pronounced in the constant-gradient than in the constant-impedance structure (see Fig. 6-14). This problem was first pointed out in Reference 4 and will be discussed in greater detail at the end of this section.
6. At the time the two-mile accelerator was being designed, the cumulative, multisection type of beam breakup described in detail in Chapter 7 was not known. On the other hand, experiments done at Stanford and elsewhere[5–8] had shown that the constant-gradient structure was relatively less troubled by the regenerative type of beam breakup than the constant-impedance structure. Various laboratories had reported beam breakup thresholds which were typically of the order of 300 mA with a 2-μsec pulse length for an S-band constant-impedance structure. At Stanford, it had been found that the instability could be triggered in a constant-impedance section with a current of 70 mA by injecting about 800 W of power at 4326 MHz backward into the output of the accelerator. However, the same result had not been achieved with an equal amount of power injected into a constant-gradient section of the same length, showing that the

Table 6-3 Comparison of constant-gradient and constant-impedance accelerator structures

Characteristic	*Constant gradient*	*Constant impedance*	*Ratio*[a] $\frac{g.c.}{c.i.}$
$\frac{E_0}{V_0/l}\left(\frac{\text{Peak elec. field}}{\text{Avg. elec. field}}\right)$	1.00	1.31	0.76
$\frac{(dP/dz)_{z=0}}{(dP/dz)_{z=l}}$	1.00	3.13	0.32
V_0 (no-load energy)	22.34 GeV	22.04 GeV	1.01
$-dV/di$	35.53 GeV/A	36.41 GeV/A	0.98
V (at $i = 50$ mA)	20.56 GeV	20.22 GeV	1.02
η_{max} (maximum beam-conversion efficiency)	0.73	0.70	1.05
$i_{\eta_{max}}$	314.2 mA	302.6 mA	1.04
v_g/c (normalized group velocity)	$0.0204 \rightarrow 0.0065$	0.0121	$1.68 \rightarrow 0.54$
t_F (filling time)	0.83 μsec	0.83 μsec	1.00
U (stored energy)	2372 J	2372 J	1.00
$\Delta_{z=l}$ (phase shift for $\delta f = 0.1$ MHz)	0.52 rad	0.52 rad	1.00
$\delta V_0/V_0$ (for $\delta f = 0.1$ MHz)	0.033	0.039	0.85

Assumed parameters:
$\tau = 0.57$
$P_{0T} = 5320$ MW (90% of which enters accelerator)
$L = 10{,}000$ ft (94.8% effective)
No. of sections = 960
$f = 2856$ MHz
$r = 53$ megohms/meter
$Q = 13{,}000$

[a] c.g.—constant gradient; c.i.—constant impedance.

Figure 6-14 Shapes of input and output RF pulses in constant-gradient (C.G.) and constant-impedance (C.I.) accelerator sections. Length of section = 10 ft, $\tau = 0.57$, and $2\pi/3$ mode in each case. Rise time of input pulse ≈ 0.1 μsec; time scale = 0.2 μsec/cm.

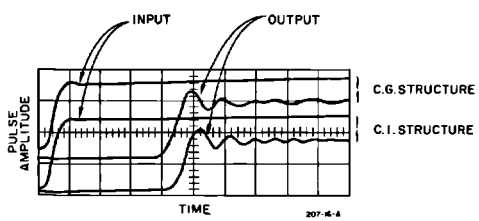

threshold must have been higher. An experiment done elsewhere[9] showed that by using a 5-ft long section of the Stanford constant-gradient design, thresholds as high as 600 mA in 3 μsec had been observed. All these results were qualitatively understood at the time in terms of the HEM_{11} dispersion diagrams which had been obtained and appear in Fig. 7-29. Indeed, in the backward-wave oscillator model, the frequency at which the $v_p = c$ line intersects the HEM_{11} dispersion diagram changes over a wide band along a 10-ft section, rather than being constant as in the constant-impedance structure. Thus buildup of the backward-wave instability is less likely to occur. Furthermore, since the currents planned at SLAC were much lower than the observed thresholds, it appeared that the constant-gradient design was assured of a reasonable degree of conservatism. As will be discussed in Chapter 7, if the accelerator were to be redesigned today, one would probably stagger accelerator sections of different designs along the 2-mile length in order to shorten the cumulative HEM_{11} interaction length at any given frequency. However, even with hindsight, it can be said that the choice of the constant-gradient design per se was correct from the beam breakup point of view since use of the constant-impedance structure, with uniform interaction along each 10-ft length, would have resulted in multisection breakup thresholds at even much lower currents than have been observed at SLAC.

The advantages of the constant-gradient accelerator discussed above had to be weighed against two disadvantages: (a) Nonuniform modular dimensions made the cavities in the constant-gradient structure more expensive to fabricate and to test. An economic comparison of the two structures showed that fabrication of the constant-gradient structure cost approximately 10% more per unit length than the constant-impedance structure. (b) At the time when the selection had to be made, there had been less operational experience with the constant-gradient structure than with the uniform structure.

It was concluded that the advantages of the constant-gradient structure outweighed its slightly higher fabrication cost. The constant-gradient structure was thus adopted for the two-mile accelerator. Subsequently, high-power tests and actual beam tests conducted with sections installed in the Mark IV and Mark III accelerators confirmed the theoretically predicted performance.

Choice of attenuation parameter (RBN)

The attenuation parameter is defined as the net attenuation in nepers in an accelerator section caused solely by resistive wall losses. It is equal to the product of the voltage attenuation per unit length and the length of the accelerator section and is designated by the symbol τ. As stated previously, $\tau = \omega t_F/2Q$, where ω is 2π times the operating frequency, t_F is the filling time, and Q is the loss factor in the RF structure. As will be evident in the following

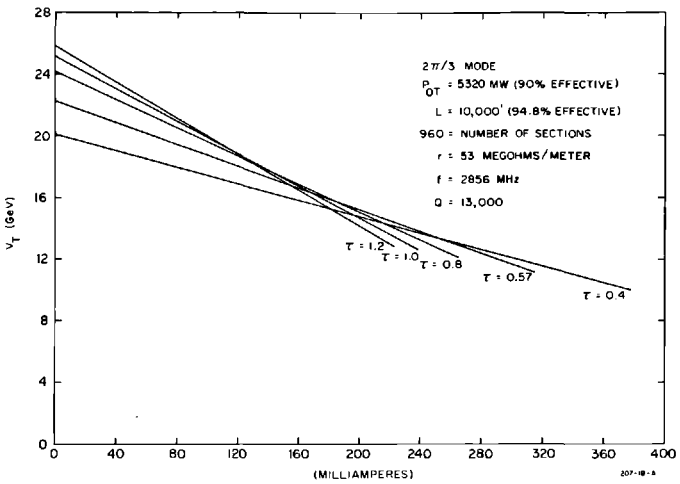

Figure 6-15 Beam loading curves for constant-gradient accelerator at various values of the attenuation parameter τ.

discussion, the value of τ influences the performance of a linac in many ways and, therefore, the proper choice of this parameter was quite important in the design of the two-mile accelerator.

The total steady-state energy gain V_T in a constant-gradient accelerator of total length L and shunt impedance r_0 is given[3] by

$$V_T = (1 - e^{-2\tau})^{1/2}(P_T L r_0)^{1/2} - \frac{i r_0 L}{2}\left(1 - \frac{2\tau e^{-2\tau}}{1 - e^{-2\tau}}\right) \qquad (6\text{-}7)$$

where P_T is the total input RF power, i is the peak beam current, and r_0 is the shunt impedance per unit length.

The first term on the right in Eq. (6-7) is the no-load energy (i.e., the electron energy at negligible current), and the second term gives the reduction in energy caused by beam loading. The reduction of energy is linear with increase in beam current, as shown in Fig. 6-15. In plotting these curves it is assumed that the electrons are situated at the peak of the traveling wave.

In the discussion which follows, the effect of τ upon the constant-gradient accelerator performance will be considered. The various accelerator characteristics are shown numerically in Table 6-4 for several values of τ.

BEAM LOADING CHARACTERISTICS. Beam loading curves for the various values of τ under consideration are shown in Fig. 6-15. The terminal point on each curve is the beam current resulting in maximum transfer of RF power to the beam. As noted, the slope $(-dV/di)$ of the beam loading curves decreases in magnitude as τ decreases. Since electrons with energies from V_{T0} to V_{Ti} emerge from the accelerator during the transient period, lower values of τ are preferred to reduce the energy spread.

Table 6-4 Calculated performance of constant-gradient accelerator at various values of attenuation parameter τ

	$\tau(Np)$				
Characteristic	0.4	0.57	0.8	1.0	1.2
(V_{To}) Unloaded energy (GeV)	20.10	22.34	24.20	25.18	25.82
($-dV/di$) Beam loading derivative (GeV/A)	26.59	35.53	45.58	52.61	58.24
(V_{Ti}) Energy at 50-mA beam current (GeV)	18.76	20.56	21.92	22.56	22.92
(ΔV)$_t$ transient energy spread (in GeV) between $i = 0$ and $i = 50$ mA	1.34	1.78	2.28	2.62	2.90
($i_{\eta max}$) Beam current at maximum conversion efficiency (mA)	377.8	314.2	265.4	239.4	221.6
(ΔV)$_e$ Energy loss in idle 10-ft section at $i = 50$ mA (MeV)	1.32	1.76	2.26	2.60	2.88
(v_g/c) Normalized group velocity[a]	0.0252–0.0113	0.0204–0.0065	0.0174–0.0035	0.0160–0.0022	0.0152–0.0014
(t_F) Filling time (μsec)	0.58	0.83	1.16	1.45	1.74
($-\delta V/V$) Energy loss for $\delta f = 0.1$ MHz	0.018	0.033	0.056	0.077	0.098

Assumptions:
$2\pi/3$ mode, constant-gradient design
$P_{OT} = 5320$ MW (90% of which enters accelerator)
$L = 10{,}000$ ft (94.8% effective)
No. of sections = 960
$f = 2856$ MHz
$r = 53$ megohms/meter
$Q = 13{,}000$

[a] The group velocity in each 10-ft accelerator section varies linearly between the limits given in each column.

MAXIMUM CONVERSION EFFICIENCY. The maximum conversion efficiency of RF power to beam power is given[3] by

$$\eta_{max} = \frac{1}{2}\left[\frac{(1 - e^{-2\tau})^2}{(1 - e^{-2\tau}) - 2\tau e^{-2\tau}}\right] \tag{6-8}$$

Maximum conversion efficiency occurs when the beam current reaches the value[3]

$$i_{\eta max} = \left(\frac{P_T}{r_0 L}\right)^{1/2}\left[\frac{(1 - e^{-2\tau})^{3/2}}{(1 - e^{-2\tau}) - 2\tau e^{-2\tau}}\right] \tag{6-9}$$

in which case the beam energy is equal to one-half of the no-load energy.

ENERGY LOSS AND POWER INDUCED WHEN THE BEAM PASSES THROUGH SECTIONS NOT SUPPLIED WITH RF POWER. When one of the klystrons along the accelerator becomes defective, it is desirable to be able to continue operation while the klystron is being changed. The amount (ΔV_e) by which the electron beam energy is reduced by excitation of an idle accelerator section of length l and the induced power P_e in this section is given[3] by

$$(\Delta V)_e = \frac{ir_0 l}{2}\left(1 - \frac{2\tau e^{-2\tau}}{1 - e^{-2\tau}}\right) \tag{6-10}$$

$$P_e = i^2 r_0 l\left(\frac{\tau^2}{e^{2\tau} - 1}\right)$$

The energy loss increases as τ increases, as shown in Table 6-4. Since each RF source supplies four accelerator sections during Stage I operation, the total energy loss given by Eq. (6-10) must be multiplied by 4. This loss must, of course, be added to the loss of beam energy incurred by the loss of the klystron (about 80 MeV under normal operating conditions).

GROUP VELOCITY. In the constant-gradient accelerator, the group velocity decreases linearly with distance along the accelerator section. It is given[3] by

$$v_g = \frac{\omega l}{Q}\left[\frac{1 - (z/l)(1 - e^{-2\tau})}{1 - e^{-2\tau}}\right] \tag{6-11}$$

FILLING TIME. A small filling time is desirable to allow the maximum available portion of the RF pulse length for the acceleration of electrons. The filling time is given[3] by

$$t_F = \frac{2Q}{\omega}\tau \tag{6-12}$$

Values of filling time for the various cases are given in Table 6-4.

FREQUENCY SENSITIVITY. The fractional beam energy loss from a fractional frequency shift $\delta f/f$ is given[3] by

$$\frac{\delta V_0}{V_0} = \left(Q\frac{\delta f}{f}\right)^2\left[\frac{2\tau e^{-2\tau}(\tau + 1)}{1 - e^{-2\tau}} - 1\right] \tag{6-13}$$

Values of $\delta V_0/V_0$ are shown in Table 6-4 for $\delta f = 0.1$ MHz.

CONCLUSIONS. From Table 6-4 it was clear that there were several advantages to using a reduced attenuation parameter τ. Except for the reduction in beam energy, the use of a low value of τ resulted in improvement of all of the factors measuring the performance of the accelerator. Moreover, the percentage improvement of each of these factors resulting from a given reduction

in τ usually exceeded the percentage loss in beam energy. In fact, if it were not for the paramount importance of high beam energy in particle physics research, the adoption of an even lower value of τ would clearly have been indicated. In conclusion, the choice of $\tau = 0.57$ was made on the basis of broad considerations, including reference to such tabulations as shown in Table 6-4, the prospective requirements of physics research, and previous accelerator experience.

[The original basis for the exact value of $\tau = 0.57$ was that this particular value resulted in a no-load energy in the constant-impedance accelerator of 10% less than the maximum no-load energy which can be obtained (occurring at $\tau = 1.26$). This was judged to be the maximum penalty in energy which one could afford to pay to obtain the advantages of low τ discussed in the text. The same qualitative reasoning held for the constant-gradient accelerator structure, and thus the value of τ selected earlier was not changed.]

Transient filter characteristics and beam loading (RHH)

PHYSICAL MODEL AND EXPERIMENTAL EVIDENCE. The band-pass filter characteristics of the accelerator structure, which were discussed briefly earlier in this chapter, will now be examined in greater detail. Both the physical model and the theory will be presented below. As already mentioned, one effect of these filter characteristics is that an impressed RF wave of finite rise time undergoes amplitude and phase oscillations as it travels down the accelerator structure. The impressed wave can come from the klystron or from beam loading. The oscillations which were illustrated in Fig. 6-14 can be understood in a simple way if one considers the symmetrical side-bands $\pm\Delta f$ of the carrier frequency (2856 MHz in this case) which are generated by the rise time of the RF wave. For an operating mode which is close to the middle of the $\omega - \beta$ diagram (see Fig. 6-21), the small side-band vectors rotate around the tip of the carrier vector in opposite directions but with approximately equal angular velocities. The resulting effect as a function of time and of distance along the structure is predominantly amplitude modulation because the sum of the two vectors remains approximately collinear with the carrier but varies in amplitude. As the operating mode gets closer to the edge of the passband, as in the $2\pi/3$ case, both amplitude and phase modulation become more apparent.

The effect of this modulation on the beam is to cause spectrum broadening. In a multisection accelerator, this spectrum broadening can be reduced by not triggering all the klystrons at exactly the same time, thereby causing the "peaks" and "valleys" to average out over a large number of sections.

Certain precautions should be taken when interpreting the pulse shapes of Fig. 6-14. It should be remembered that these pulses represent electric field amplitudes obtained at the end of a 10-ft section and that the electron beam energy results from the integral taken over the full length. Experiments done

by probing the field through small coupling holes drilled along a 10-ft section show that the evolution of the pulse shapes as a function of length is more complicated in the constant-gradient structure than in the constant-impedance structure. In addition to the side-bands caused by the rise time of the pulse, there is a frequency modulation effect. This frequency modulation is inherent in the rise time of the pulsed klystron supplying the RF power. At turn-on, the frequency can in fact be several megahertz higher than when the flat top of the modulator pulse is reached. This initial energy, which travels down the accelerator structure at a higher frequency, reaches an increasingly narrow pass-band structure as seen in Fig. 6-21. Before being attenuated, this energy travels at a group velocity which is much lower than the corresponding group velocity at 2856 MHz. When the pulse shape is examined in the middle of the section, the wiggles do not die out, i.e., the filling time is at least 2.5 microseconds long. Finally, towards the coupler end, the higher frequency energy gets attenuated or reflected and the pulse looks more and more like the simple output shown in Fig. 6-14. Because of the presence of the higher frequencies, the frequency of the wiggles is about twice as high at the input as at the output. While this effect is probably unimportant, experiments have shown that a 50% reduction in ripple amplitude can be obtained if a diode modulator at low power, preceding the klystron, is used for RF turnon. This result can be understood by the reduction in frequency modulation obtained with the *p-i-n* diode as compared with the klystron alone.

COUPLED RESONATOR WAVE EQUATIONS. The transient phenomena of wave propagation and beam loading can be described approximately by a simple theory in which the disk-loaded waveguide is treated as a continuous transmission line of which the dispersive properties are characterized by a well-defined group velocity. As has been pointed out by J. Leiss,[4] however, such

Figure 6-16 Mathematical model of a disk-loaded waveguide.

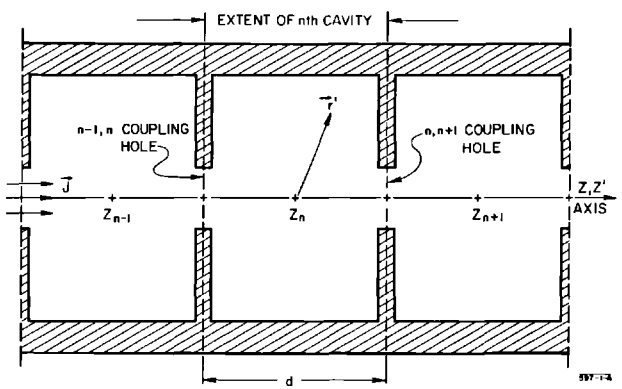

a treatment overlooks important transient effects arising from the finite passband of the periodically loaded structure.

The approach used here is an approximate version of coupled-resonator theory, equivalent to the filter-network approach of Reference 4. The wave equation may be written* (see Fig. 6-16 for geometric nomenclature):

$$\left(\frac{\partial^2}{\partial\tau^2} + 2\beta_n\frac{\partial}{\partial\tau} + \omega_n^2\right)A_n(\tau) - \omega_n\left\{\Omega_{n-1/2}A_{n-1}\left(\tau + \frac{d}{v}\right) + \Omega_{n+1/2}A_{n+1}\left(\tau - \frac{d}{v}\right)\right\}$$
$$= \frac{4\pi}{u_n}\int_{\text{cavity}} \psi_{zn}^*(\mathbf{r}')J_z\left(\mathbf{r}', \tau - \frac{z'}{v}\right)d^3\mathbf{r}' \quad (6\text{-}14)$$

where

$A_n(\tau)$ is related to the vector potential in the nth cavity by $\mathbf{A} \approx A_n(\tau)\psi_n(\mathbf{r}')$,
$\psi_n(\mathbf{r}')$ is the characteristic spatial distribution of the vector potential in the nth cavity,
$\psi_{zn}(\mathbf{r}')$ is the z-component of ψ_n,
$\tau \equiv t - \int_0^{z_n} dz/v(z)$ is the "local" time, retarded by electron transit time,
ω_n is a characteristic frequency parameter (the midband frequency),
$\beta_n = \frac{1}{2}\omega_n/Q_n$ is the loss coefficient,
$\Omega_{n\pm1/2}$ is a measure of the coupling between the nth and $(n \pm 1)$th cavities,
$u_n \equiv \int_{\text{cell}} |\psi_n(\mathbf{r}')|^2\, d^3\mathbf{r}'$ (proportional to stored energy); and
$J_z(\mathbf{r}', \tau)$ is the current density, assumed to consist of electrons traveling in the $\pm z$ direction at velocity v.

The assumptions that the parameters β_n, ω_n, and Ω_n are simple scalers is strictly valid only in the weak-coupling (small-hole) limit.

The equation may be interpreted phenomenologically by noting that, if the parameters vary only adiabatically as a function of n, then the homogeneous part has solutions of the form

$$A_n \approx A_{n-1}e^{-ik_n d}$$

where an implicit $e^{i\omega\tau}$ is understood, and

$$\omega_n^2 + 2i\beta_n\omega - \omega^2 \approx 2\omega_n\Omega_n\cos k_n d \quad (6\text{-}15)$$

Thus, if one assumes

$$\beta_n \ll \omega_n \quad \text{and} \quad \Omega_n \ll \omega_n$$

the dispersion formula is a cosine-like curve with ω_n the midband frequency and Ω_n approximately the half-bandwidth.

* In the present discussion, the units are Gaussian with $c = 1$, unless otherwise noted.

An even simpler dispersion relation results if one assumes $|(\omega-\omega_n)/\omega_n| \ll 1$; i.e., that the fields have no frequency components very far from $+\omega_n$; one may then write

$$\omega_n + \beta_n - \omega \approx \Omega_n \cos k_n d \tag{6-16}$$

In this case the wave equation may be written

$$\left(\frac{\partial}{\partial\tau} + \beta_n - i\omega_n\right)A_n(\tau) + \frac{i}{2}\left\{\Omega_{n-1/2}\,A_{n-1}\left(\tau + \frac{d}{v}\right) + \Omega_{n+1/2}\,A_{n+1}\left(\tau - \frac{d}{v}\right)\right\}$$

$$\approx \frac{2\pi}{i\omega_n u_n}\int_{\text{cavity}} \psi^*_{zn}(\mathbf{r}')J_z\left(\mathbf{r}', \tau - \frac{z'}{v}\right) d^3\mathbf{r}' \tag{6-17}$$

APPLICATION TO ACCELERATOR MODE. In the accelerator mode, the longitudinal field is transversely uniform near the axis, e.g.,

$$\psi_z \approx \psi_z(0, 0, z')$$

Defining the complex voltage gain, $w_n(\tau)$, by

$$w_n(\tau) = \int_{\text{cavity}} E_z\left(\tau + \frac{z'}{v}\right) dz' \tag{6-18}$$

or, assuming an instantaneous variation $\sim e^{i\omega_n\tau}$, and noting that $E_z \approx -i\omega_n A_z$, one may write

$$w_n(\tau) \approx -i\omega_n F_n A_n(\tau) \tag{6-19}$$

where

$$F_n = \int_{\text{cavity}} \psi_z(z')e^{i\omega_n z'/v}\, dz' \tag{6-20}$$

The voltage gain for an electron entering the structure at time $t = \tau$ is

$$V(\tau) = \sum_1^N \text{Re}\, w_n(\tau) \tag{6-21}$$

The wave equation (Eq. 6-17) may now be written

$$\left(\frac{\partial}{\partial\tau} + \beta_n - i\omega_n\right)w_n(\tau) + \frac{i}{2}\{\tilde{\Omega}_{n-1/2}\,w_{n-1}(\tau) + \tilde{\Omega}_{n+1/2}\,w_{n+1}(\tau)\} \approx -\beta_n R_n I(\tau) \tag{6.22}$$

where $I(\tau)$ is the beam current;

$$\tilde{\Omega}_{n\pm1/2} = \Omega_{n\pm1/2}\,e^{\mp i\omega_n d/v}$$

and R_n, the shunt impedance per cavity, is defined by

$$\frac{R_n}{Q_n} = \frac{2\beta_n R_n}{\omega_n} = \frac{4\pi}{\omega_n}\frac{|F_n|^2}{u_n} \tag{6-23}$$

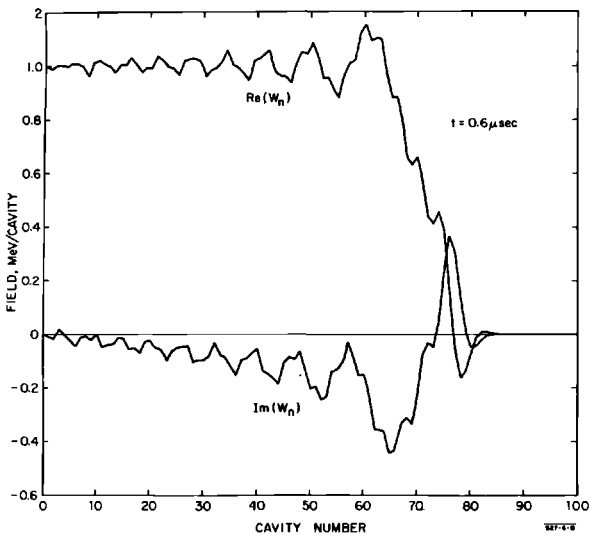

Figure 6-17a Field distribution in the accelerating mode along a constant-gradient structure, 0.6 μsec after turning on a unit step-function driving voltage in the zeroth cavity.

The transient behavior of typical disk-loaded guides has been investigated by a computer program which integrates Eq. (6-22). The program data input provides for arbitrary longitudinal variation of the waveguide parameters and choices of appropriate boundary conditions, driving sources, and beam models. As a computational convenience, the program actually calculates the function $W_n(\tau)$, defined by

$$w_n(\tau) = W_n(\tau)e^{i\omega'\tau}$$

where ω' is a constant reference frequency (e.g., the driving source frequency) and $W_n(\tau)$ is slowly varying in phase and amplitude.

Figures 6-17 and 6-18 show the results of typical computations based on the properties of the SLAC structure. The table below summarizes the pertinent initial and final values of the parameters:

Cavity No.	v_g/c	$\Omega/2\pi$ *(MHz)*	Q	R/d *(megohms/meter)*
0	0.0204	32.0	14,170	53
85	0.0061	10.41	13,220	60

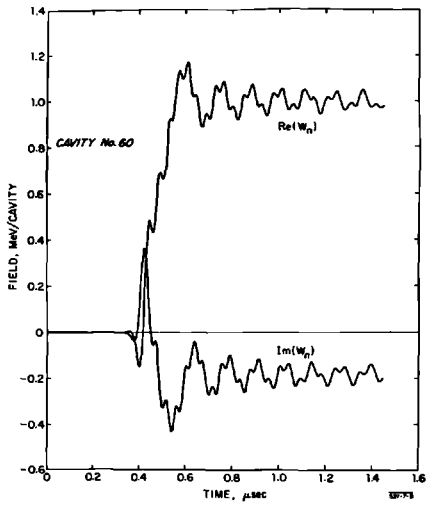

Figure 6-17b Arrival of the RF pulse at cavity No. 60 (6.9-ft point).

Figure 6-17c Arrival of the RF pulse at the 10-ft point. Note increased dispersion of the initial rise, as compared to Fig. 6-17b. The substantial out-of-phase component results from an error of ≈0.06 MHz in entering the mid-band frequency in the program input data.

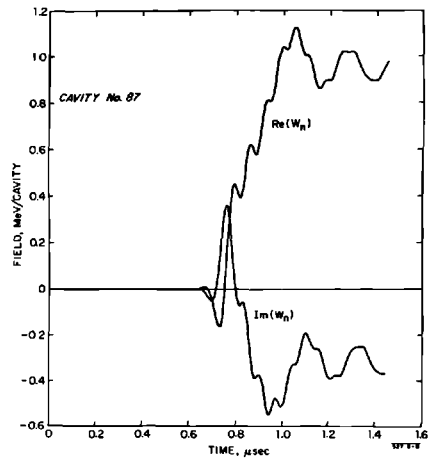

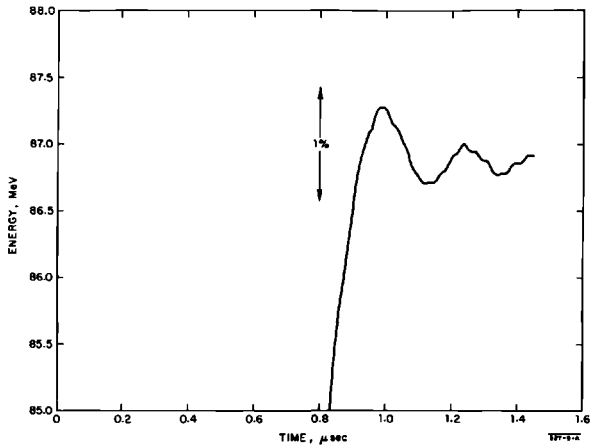

Figure 6-18 Electron energy gain versus time corresponding to the case of Figs. 6-17a, b, and c. The large ripples seen in the field plots have nearly averaged out in the summation over the cavities.

The values of half-bandwidth, Ω_n, used in the computation are derived from the design group velocity, $v_g(n)$, through the relation

$$v_g = \frac{\partial \omega}{\partial k} \approx \Omega\, d \sin k\, d$$

A step-function driving voltage applied at time $\tau = 0$ at the input boundary was assumed in all the computations. Physically, such a step function would be closely approximated by means of the *p-i-n* diode mentioned earlier. It is seen that these computations are in excellent agreement with the experimental observations mentioned above. Comparing Figs. 6-17b and 6-17c, it is seen how the wiggles evolve as a function of length, as the group dispersion increases. As the pass-band becomes narrower, certain frequency components which are shock-excited by the step-function driving voltage are reflected from the 0- or π-mode band edge at some point down the structure, propagate back to the input where they are again reflected by the constant voltage source (zero impedance) and thus set up standing-wave resonances. Such resonances would probably be much less noticeable in a more realistic case with finite rise time and source impedance matched to the guide. The appearance of a significant out-of-phase component of the field (Fig. 6-17c) results from a slight input data error of $\approx$0.06 MHz in the midband frequency. As a result, the wave is not quite synchronous at the assumed bunching frequency of 2856 MHz.

In conclusion, it is seen from Fig. 6-18 that the variation in electron energy gain is at most 1% at the beginning of the beam pulse and that it rapidly decreases from then on. Measurements made with a short accelerator length have confirmed these results.

6-2 Empirical design of the accelerator structure

Choice of the disk-loaded waveguide (GAL)

The first section of this chapter was concerned with the general determination of accelerator parameters. This section describes the procedures used to design empirically an accelerator structure that satisfies the above parameters.

The disk-loaded waveguide is not the only slow-wave structure capable of accelerating electrons. In fact, other structures (see Fig. 6-19) such as the grid-loaded ("jungle gym") waveguide yield shunt impedances about twice that of the disk-loaded waveguide. But in every case that was examined, where a large improvement in shunt impedance was obtained, the bandwidth and resulting group velocity were at least 10 times as high as desired. Efficient utilization of the available RF power under these conditions would have

Figure 6-19 Slow-wave structures proposed for linear accelerators.

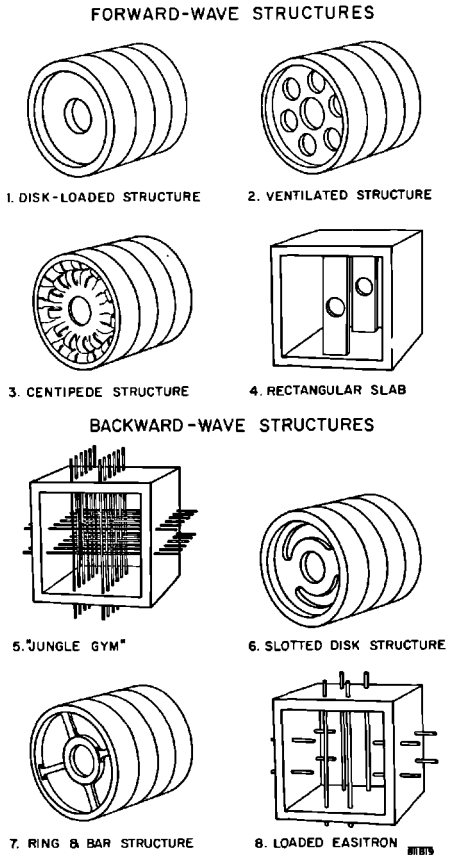

required its recirculation (feedback) or the use of extreme lengths between feeds. The former was undesirable, especially in a long multisection accelerator, because it would have resulted in undue operational complications; the latter would have required that each accelerator section transmit an excessive amount of power. Several variations of structures 2 through 8 shown in Fig. 6-19 were devised which succeeded in reducing the group velocity to the desired values (in the range of $0.01c$), but these measures also caused the shunt impedance to be reduced until no advantage remained; moreover, they would have resulted in increased cost of fabrication. For these reasons, the disk-loaded waveguide was preferred for the two-mile accelerator.

Definition and discussion of dimensions (GAL)

The modular dimensions of the disk-loaded waveguide which can be adjusted to achieve the intended parameters have already been illustrated in Fig. 6-2. Figure 6-2a and b shows the cylindrical guide diameter $2b$, the disk-hole diameter $2a$, the disk-edge radius ρ, and the land in the disk aperture s. Figure 6-2c shows further variations of the disk-loaded waveguide using so-called "conical" or "anticonical" disks. The conical disk was rejected because of its comparatively low r/Q. The anticonical disk was dismissed because of machining difficulties, although it has a 5% higher r/Q than the corresponding flat disk structure with $t = t_1 = 0.230$ in.

As indicated earlier, a 10% improvement in shunt impedance was gained by adopting the $2\pi/3$ mode rather than the $\pi/2$ mode. Figure 6-20 illustrates

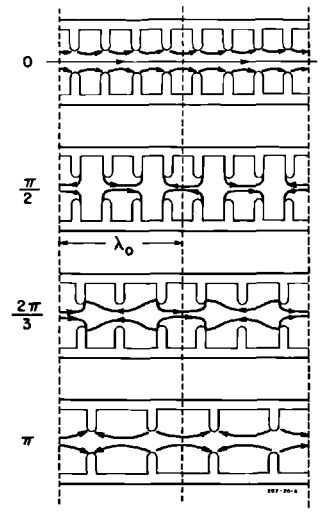

Figure 6-20 Traveling-wave electric field configurations for 0, $\pi/2$, $2\pi/3$, and π phase shift per cavity.

the respective traveling-wave field configurations at an instant in time over two wavelengths (the zero and π "standing-wave modes" are also illustrated for reference). These patterns are deformed as they slide down the waveguide but reappear in the same configuration, shifted by one cavity, at an instant $\delta t = \phi/2\pi f$ later, where ϕ is the phase shift per cavity at the frequency f.

For standard accelerator sections, the objective is to obtain a phase velocity equal to the velocity of light. Thus, specifying the operating mode and frequency (or free-space wavelength) fixes the distance between disk center lines at $d = \phi c/\omega$. After this choice, only four dimensions remain to be specified: $2b$, $2a$, ρ, and t. The lower cutoff frequency of the disk-loaded waveguide, or "zero-mode" frequency, is strongly dependent upon the waveguide diameter $2b$, whereas the bandwidth and, thus, the group velocity depend primarily on the ratio a/b at given values of ρ and t. This point is illustrated by the three ω–β (Brillouin) diagrams shown in Fig. 6–21. For experimental tests and later, in the fabrication, it was important to verify that the disk aperture edge had been properly formed; this was done through some technique such as that utilizing a steel ball (Fig. 6–2b) or a more

Figure 6-21 Brillouin diagrams for three different points in a typical constant-gradient section.

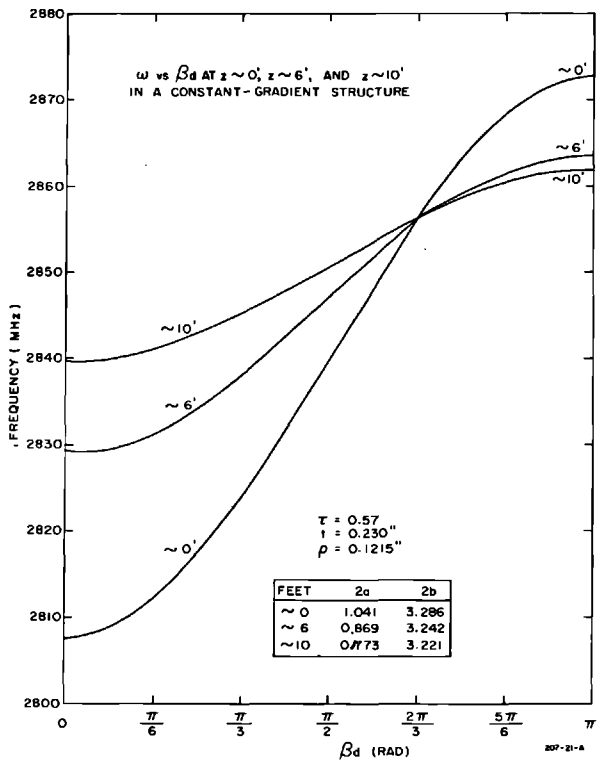

sophisticated contour plotter. Errors in the ball height h or the land s cause significant errors in the resonant frequency of test sections and hence in the resulting phase and group velocities. This fact is easily understandable because the electric field intensity is relatively strong at the disk edge. The choice of ρ can be quite arbitrary from the RF point of view so long as the tolerances are respected and electric breakdown does not result.

The choice of the disk thickness t, as discussed in the previous section, involve a compromise between the use of thin disks to increase the shunt impedance and thick disks to reduce the danger of electrical breakdown, improve heat-transfer characteristics, and increase mechanical strength.

Evolution of Stanford designs (GAL)

Prior to 1960, all Stanford accelerators had been designed to operate in the $\pi/2$ mode. Starting in 1960, the first $2\pi/3$ mode structure was tested on the 20-ft Mark IV accelerator. Until 1962, all Stanford accelerators were of the constant-impedance type. Then, in April 1962, the first constant-gradient structure was installed on the Mark IV accelerator. Finally, SLAC-type constant-gradient structures were installed on the Mark III accelerator in December 1963, replacing the earlier $\pi/2$ structures.

Table 6-5 shows a recapitulation of the respective characteristics of constant-impedance structures operating in the $\pi/2$ mode on the early Mark III accelerator and in the $2\pi/3$ mode on the Mark IV accelerator.

Table 6-5 Characteristics of Stanford constant-impedance structures

Parameters	*Mark III accelerator (1952)*	*Mark IV accelerator (1960)*
Operating mode	$\pi/2$	$2\pi/3$
Length (ft)	10	10
Waveguide inside diameter $2b$ (in.)	3.247	3.247
Disk hole diameter $2a$ (in.)	0.8225	0.890
Disk thickness t (in.)	0.230	0.230
Periodic length d (in)	1.0335	1.378
Disk edge radius ρ (in.)	0.1215	0.1215
Matching iris aperture (in.)	1.042	1.014
Frequency (MHz)	2856	2856
Group velocity v_g/c	0.0100	0.0122
Shunt impedance r_0 (megohms/meter) (corrected for fundamental space-harmonic amplitude)	47	53
Q	10,000	13,200
Attenuation τ (Np)	0.90	0.57

Constant-gradient structure dimensions (GAL)

As already discussed, the two-mile accelerator is of the constant-gradient type, propagating in the $2\pi/3$ mode. The constant field is obtained by tapering the cross-sectional dimensions of the waveguide so as to produce the required linear decrease in group velocity. The constant-field condition then results only if the shunt impedance and the Q of the cavities remain constant over the length of the section in spite of the cross-sectional variation of the structure. In practice, for a group velocity variation such as that chosen for the SLAC design, the shunt impedance r_0 (corrected for the fundamental space harmonic) increases by a small percentage over a 10-ft section, thereby yielding a structure with a gradual input-to-output field increase of 5%. Then, in the presence of beam loading, the rising field characteristic is compensated for, as will be seen later in this section.

Two constant-gradient structures were designed, one for thick disks ($t = 0.230$ in.), the other for thinner disks ($t = 0.120$ in.). Their performances were compared and the thicker disk design was chosen for the reasons already mentioned earlier. Figures 6-22 and 6-23 show the respective variations of $2b$, $2a$, v_g/c, and r_0 as a function of cavity number along a 10-ft section.

Figure 6-22 Variation of *2b*, *2a*, v_g/c, and the shunt impedance r_0 (corrected for the fundamental space harmonic) as a function of cavity number along a 10-ft constant-gradient section for $t = 0.230$ in. The values of *2b* and *2a* in this figure are those given in Table 6-6. These final values were obtained by applying several corrections to the cold test data, including those given by Eqs. (6-44) and (6-45).

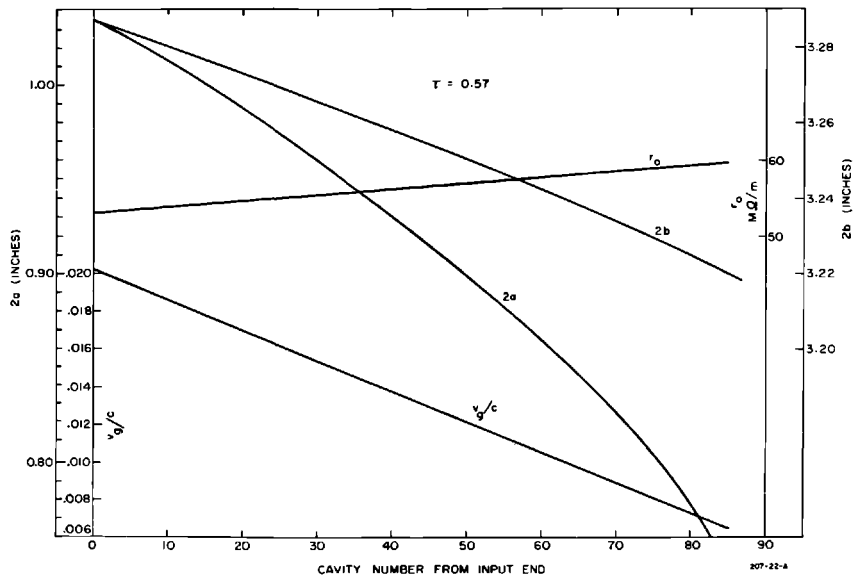

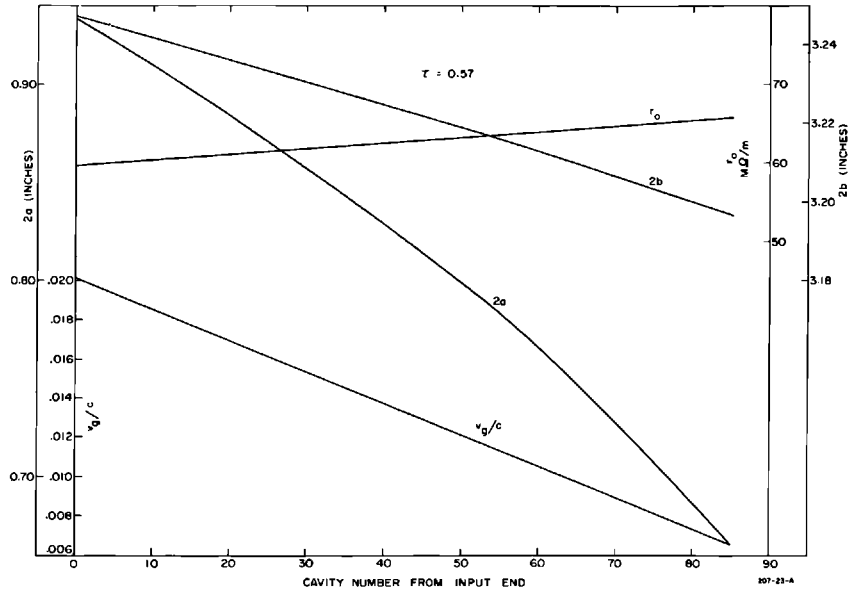

Fig. 6-23 Variation of $2b$, $2a$, v_g/c, and the shunt impedance r_0 (corrected for the fundamental space harmonic) as a function of cavity number along a 10-ft constant-gradient section for $t = 0.120$ in.

Cavities 0 and 85 are coupler cavities. It is seen that whereas $2b$ varies by less than 2%, $2a$ is reduced at the output by 30% from its input value to satisfy the group velocity variation.

When economy in fabrication is desired, a constant-gradient design can be approximated by adjusting the dimensions in steps, each step consisting of several identical cavities. However, for the two-mile Stanford accelerator, the cost of the slow-wave structure represented only a small percentage of the total cost, and the small increase incurred by varying the dimensions cavity by cavity was well justified to achieve a smooth field gradient.

Cold tests and corrections to achieve the empirical design (GAL)

OBJECTIVES AND VALIDITY OF COLD TESTS. A computer program sufficiently accurate to permit calculation of the dimensions of the constant-gradient designs shown in Figs. 6-22 and 6-23 did not exist at the time. Consequently these dimensions had to be determined experimentally from cold tests. To achieve an accurate design, a fair number of pairs of $2b$ and $2a$ values had to be determined, each set of values being obtained from a different resonant test cell. About ten different test cells were used for each of the constant-gradient designs. For each test cell, the following quantities were measured: the phase velocity v_p, the group velocity v_g, r/Q, Q, and the fundamental

space harmonic amplitude $a_0^2/\sum a_n^2$. The detailed description of these microwave measurements is beyond the scope of this book. Comprehensive treatments of this subject can, for example, be found in References 2, 10, and 11. However, a brief comment is made here on each of these measurements to outline the techniques that were used and the precautions that were taken. A discussion of the corrections applied to the experimental results is also included.

Results of cold tests on short test cells are valid if the reflection symmetries of the structure are carefully taken into account. Shorting plates must be located only in planes to which the electric-field vector is normal and in such a way that the standing wave "trapped" between them is an exact representation of the instantaneous traveling wave one wishes to study. The dotted lines in Fig. 6-20 show such planes. For observation of the $2\pi/3$ mode, sets of three or six identical cavities were used, covering one or two full wavelengths. These cavities were made of carefully machined copper or brass cups and rings, half-height rings being used at the end to apply the correct boundary conditions.

When measurements are being made, it is essential that the cavities be stacked and aligned very carefully, preferably by means of a concentric jacket, and that good electrical contact be obtained through a uniformly applied pressure.

Figure 6-24 Typical experimental setup showing cavity stack used to obtain Brillouin diagram by successive resonances.

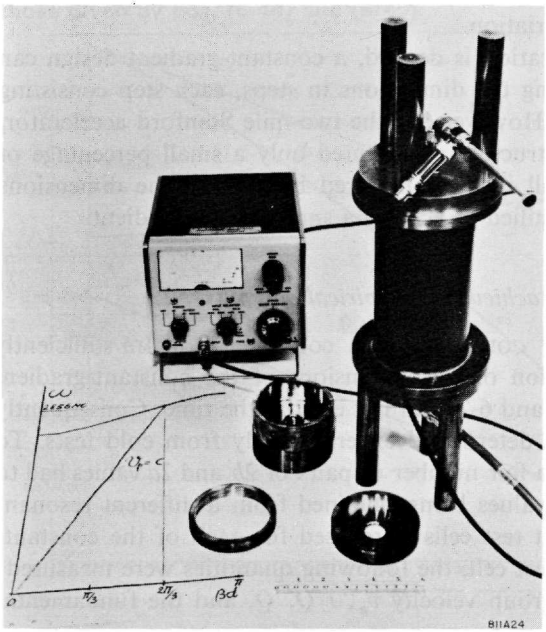

MEASUREMENT OF PHASE VELOCITY v_p. The graph in Fig. 6-24 illustrates a typical Brillouin diagram with the phase velocity $v_p = c$ for a $2\pi/3$ phase shift per cavity at $f = 2856$ MHz. The disk spacing was fixed at $\lambda/3 = c/3f = 10^4/2856$ cm. With three or six cavities of the type shown, four or seven resonant frequencies, respectively, representing $n\pi/3$ $(0 \leq n \leq 3)$ or $n\pi/6$ $(0 \leq n \leq 6)$ phase shift per cavity, can occur; these points were recorded to draw the ω–β diagram. With a moderate amount of experience, three rounds of machining correction of the diameter $2b$ were sufficient to approach the operating frequency (2856 MHz) within less than 1 MHz at $2\pi/3$ resonance. The remaining correction was done by interpolation.

MEASUREMENT OF GROUP VELOCITY v_g. The condition $v_g = c$ can be obtained for various pairs of $2b$ and $2a$ values. Each pair yields a different ω–β diagram and, hence, a different group velocity. This fact has already been illustrated in Fig. 6-21. Figure 6-25 shows the two cavity stacks for the extreme cases, the first and the last cavities of the constant-gradient section. The differences in $2a$ for $v_g/c = 0.0204$ and $v_g/c = 0.0065$ can be observed. To obtain the group velocity, the slope of the ω–β diagram was measured and, for better accuracy, a Stirling or Fourier approximation formula[12] was used with the measured resonance frequencies.

Figure 6-25 Typical cold test setup showing cavity stacks and group velocity variation as a function of length along a constant-gradient section.

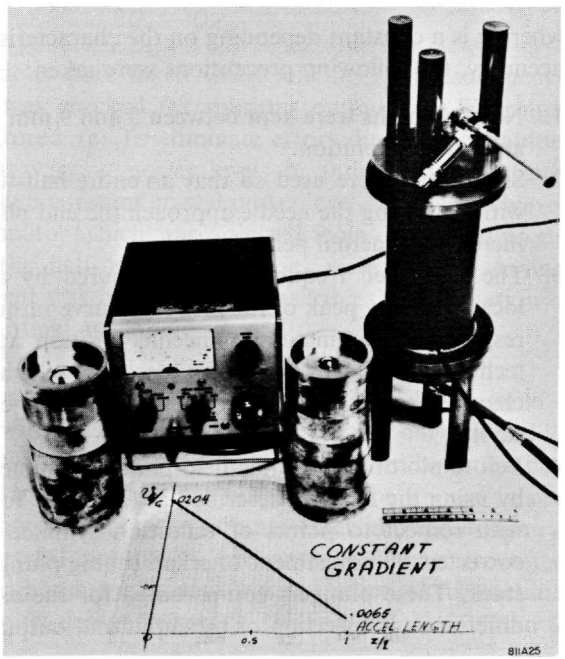

MEASUREMENT OF r/Q. The ratio of shunt impedance per unit length to Q was best measured by perturbing the axial fields in the cavity stack with a thin dielectric rod and by measuring the resonant frequency perturbation Δf. Using Slater's perturbation formula,[11,13] the value of $(r/Q)_T$ (where the index T denotes the sum of all space-harmonic components) is given by

$$\left(\frac{r}{Q}\right)_T = \frac{240c}{(\varepsilon - 1)A}\frac{\Delta f}{f^2} \tag{6-24}$$

where ε is the dielectric constant of the rod (for sapphire $\varepsilon \approx 10$), and A is its cross-sectional area. It was easiest to calibrate the dielectric rod in a simple TM_{010} cavity, for which r/Q can be calculated.

MEASUREMENT OF THE SPACE-HARMONIC AMPLITUDE. Since only the fundamental space harmonic propagates at $v_p = c$, it alone gives a net energy gain to the electrons. Thus, to obtain the effective $(r/Q)_0$, it was necessary to obtain the amplitude of the fundamental. The figure of merit by which to multiply $(r/Q)_T$ to obtain $(r/Q)_0$ is $a_0^2/\sum a_n^2$, the ratio of the square of the fundamental harmonic amplitude divided by the sum of the squares of all harmonic amplitudes. This ratio was obtained by noting the frequency perturbation caused by a short metallic or dielectric needle drawn along the axis of the resonant cavity stack. The field E_c at a given axial position in the cavity is related to the frequency perturbation Δf caused by the needle located in that position by

$$E_c^2 = k\,\Delta f \tag{6-25}$$

where k is a constant depending on the characteristics of the needle. For best accuracy, the following precautions were taken:

1. Needle lengths were kept between 5 and 9 mm to give adequate sensitivity and good resolution.
2. Six cavities were used so that an entire half-wavelength could be probed without letting the needle approach the end plates, where its image would increase the actual perturbation.
3. The perturbed frequency was measured by adjusting the frequency to locate the new peak of the response curve rather than by observing power response as a function of needle position at constant frequency. This technique avoided the difficulties[14–16] which arise from simultaneous changes in the resonant frequency and the coupling coefficients of the cavity.
4. Before plotting the whole field pattern, symmetry of the field was checked by using the method described in (3) above for a few points symmetrical with respect to points of reflection symmetry. Lack of symmetry was corrected by adjustment of small tuning plungers at the top of the cavity stack. These plungers compensated for the asymmetry created by slight differences in insertion of the input and output coupling loops.

After the field pattern was obtained, a Fourier analysis was carried out to obtain the figure of merit, which is given by

$$\frac{a_0^2}{\sum a_n^2} = \frac{1}{\lambda} \frac{\left(\int_0^{\lambda/2} E_c \cos(2\pi/\lambda)z \, dz\right)^2}{\int_0^{\lambda/2} E_c^2 \, dz} \tag{6-26}$$

It was sufficient to divide the E_c pattern into twenty-one intervals and evaluate the integral using the trapezoidal approximation.

MEASUREMENT OF Q. This was the most difficult measurement to make because the results depended on the state of the metal surface and the degree of contact between cavities. Measurements were usually taken immediately after electropolishing the cavities. Using very weak coupling, the Q's of three-cavity (Q_3) and six-cavity (Q_6) sets were successively obtained by the half-power point technique:

$$Q = \frac{f}{\Delta f} \tag{6-27}$$

where f is the resonant frequency and Δf is the frequency variation between half-power points. Although the Q's thus obtained were lowered by end-plate losses, the end effects were eliminated through use of the following expression[11]:

$$Q = \frac{Q_3 Q_6}{2Q_3 - Q_6} \tag{6-28}$$

The following precautions were taken when making Q measurements: (a) The signal generator was checked for spurious outputs. (b) The input power was carefully monitored. (c) To eliminate errors due to uncertainties in crystal law behavior at varying power levels or indicator calibrations, measurements were made at a constant crystal power level. This was achieved by using a precision attenuator which was adjusted from 3 to 0 dB as the resonant frequency and the half-power frequencies were sought. A final check of the Q measurement was obtained by measuring the attenuation of an accelerator section after final assembly.

ENVIRONMENTAL TEST CONDITIONS AND CORRECTIONS. In order to build a constant-gradient section with fixed t, d, and ρ dimensions, only $2b$ and $2a$ had to be obtained and their relationship with v_p and v_g had to be determined accurately. The quantities $(r/Q)_0$ and Q did not have to be known so precisely, because to a first approximation they do not enter into the design.

Measurements were carried out in an environment having accurately controlled temperature and humidity. Since it was not practical to machine-test cavities to attain the exact design frequency, the final value of $2b$ had to

be corrected for the residual Δf. It was usually sufficient to base the correction on the simple relation

$$\frac{\Delta 2b}{\Delta f} \approx -\frac{2b}{f} = -0.0011 \text{ in./MHz (at 2856 MHz)} \tag{6-29}$$

Another correction was required to arrive at the operating frequency for a given copper temperature differing from the room temperature at which the tests were being performed. In addition, most cold tests were done in air, and a correction had to be applied for the dielectric constant of air, which is a function of the ambient humidity and temperature (see Adam's nomograph in any engineering handbook). These problems were not very critical for short cavity-stack measurements but became important during matching and tuning operations, as discussed in a later section. For copper, the following rule of thumb can be applied at 2856 MHz:

$$\frac{\Delta f}{\Delta T} = -0.100 \text{ MHz}/2^\circ\text{C} \tag{6-30}$$

Translation from air at 80°F and 40% humidity to vacuum results in a frequency increase of about 300 parts/million.

Having applied these corrections, the values of $2a$ and $2b$ were smoothed, first by plotting the points on a curve, and then by using a simple computer program to obtain a fourth-order fit.

Basic considerations in matching and tuning an accelerator section (GAL)

If the process of machining parts and fabricating an accelerator structure could be carried out with perfect accuracy, a section such as the one shown in Fig. 5-13 would be ready for installation and use immediately after fabrication.

In practice, however, it is difficult to control the process of manufacturing to this extent; moreover, it is not economical to do so. By relaxing the tolerances on the fabrication techniques described later in this chapter, it was possible to reduce the cost of the accelerator considerably. The imperfections were corrected through the process of tuning and matching for a relatively small incremental cost.

The process of tuning an accelerator section consisted of applying external mechanical pressure to impart a permanent deformation to the wall of any cavity of which the phase shift differed from the design value. In tuning, a maximum phase excursion of $\pm 2.5^\circ$ was allowed for the 10-ft sections of the two-mile machine.

Matching the couplers of an accelerator section was done by adjusting the dimensions of the input and output coupling irises (see Fig. 6-26) so as to insure a low standing-wave ratio at the input and output of the structure. An upper VSWR limit of 1.05 was set as the matching requirement for all couplers. The main technical difficulty stemmed from the fact that the processes of

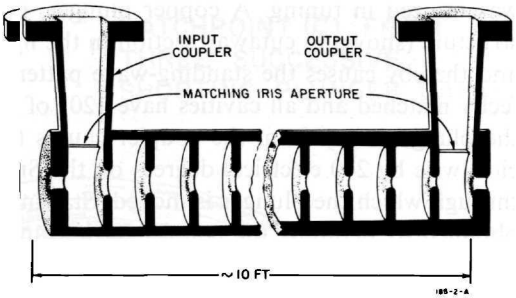

Figure 6-26 Sketch of a 10-ft long, constant-gradient, accelerator structure with input and output couplers. Notice slight taper in modular dimensions (diameter of inner wall).

tuning and matching are interrelated; the shape of the coupling iris determines both the coupling to and the phase shift of the first cavity.

A complete description of the theory and operations involved in tuning and matching an accelerator section is beyond the scope of this chapter. Good discussions on these subjects can be found in References 2, 10, 11, and 17–19. Only a few of the general principles and relevant precautions are given below.

Although the simplest mode to tune and match is the $\pi/2$, any submultiple of 2π, such as the $2\pi/3$ mode, can be handled without undue difficulty.

Figure 6-27 illustrates the principle of the nodal-shift technique which

Figure 6-27 Principle of the nodal shifting technique. Shown at left are the cutaway section with the copper plunger, and typical Smith chart plot.

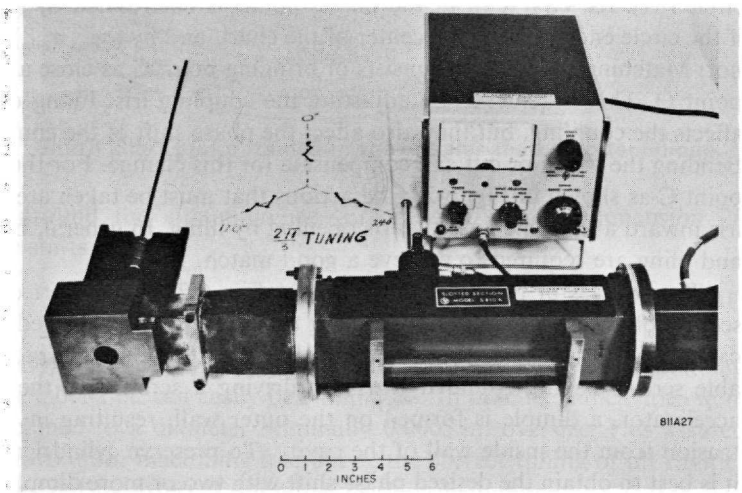

was utilized in tuning. A copper plunger, progressively pulled through the structure (shown in cutaway section in the figure), detunes successive cavities and thereby causes the standing-wave pattern to shift. If the coupler is perfectly matched and all cavities have 120° of phase shift ($2\pi/3$ mode), pulling the plunger away from the coupler causes the plotted null points to rotate clockwise by 240 electrical degrees on the Smith chart for each cavity length through which the plunger is moved. Starting from the reference point of 0°, obtained by detuning the coupler cavity (and, hence, representing the plane of the iris), the points move clockwise as shown in Fig. 6-27 from 0° to 120°, from 120° to 240°, from 240° to 0°, and so on. For the first cavities, the VSWR is nearly infinite and the points are on the rim of the chart. Farther down the section, the VSWR decreases because of the increasing net attenuation between the input of the section and the short. Thus, the plotted points move toward the center of the chart along the three radii, shown as dashed lines in Fig. 6-27. With the coupler perfectly matched but the cavities not exactly tuned, the points move erratically toward the center, as shown by the heavy lines. However, the center of the circle passing through three consecutive points still coincides with the center of the chart. When a systematic phase-shift error exists, because of an inaccurate choice of frequency, the points spiral in toward the center, clockwise if the phase shift is too large (frequency too high), or counterclockwise if it is too small (frequency too low). If the coupler is mismatched (see Fig. 6-28), the circle passing through the three points is no longer concentric with the rim of the chart. It now has two "centers"—a geometrical center and a "Smith center." Neither coincides with the center of the chart. The Smith center is the point that would be obtained if the perfectly reflecting plunger were replaced by a perfectly matched load. It can be determined mathematically[10,11] from geometric considerations. The match point (C) will lie on the extension of the straight line from the center of the Smith chart (O) to the geometric center of the circle (M). Its VSWR (σ at the match point) is determined by $(\sigma_{max}/\sigma_{min})^{1/2}$ if the circle encompasses the center of the chart, and by $(\sigma_{max}\,\sigma_{min})^{1/2}$ if it does not. Matching the coupler consists of bringing point C as close as possible to point O. This is achieved by adjusting the coupling iris. Filing or squeezing affects the coupling, but they also affect the phase shift of the coupling cavity. Bending the iris in or out can compensate for this change. For the example of point C as shown in Fig. 6-28, the actions that must be taken are to bend the iris inward and to increase the iris opening by filing. In general, both bending and filing are required to achieve a good match.

The process of tuning is illustrated in Fig. 6-29 for a short experimental section of accelerator pipe. The tuning tool here is being applied to the third cavity. It consists of a demountable collar with two or three radially adjustable screws having rounded ends. By driving a screw into the wall of the accelerator, a dimple is formed on the outer wall, resulting in a small protrusion from the inside wall of the cavity. To preserve cylindrical symmetry, it is best to obtain the desired phase shift with two or more dimples uniformly

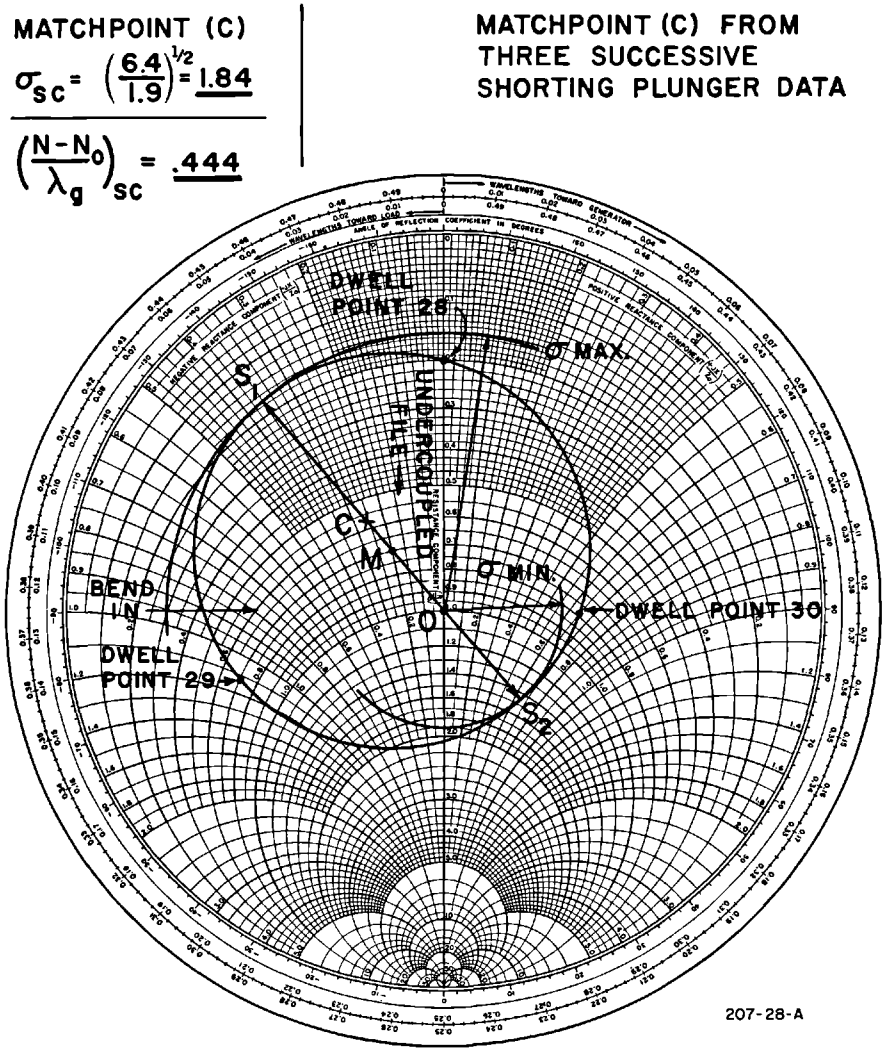

Figure 6-28 Smith chart plot obtained in the coupler-matching technique.

distributed around the circumference. Errors $\Delta(2b)$ in the dimension $2b$ create phase shifts $\Delta\phi$ by

$$\Delta\phi = \frac{2\pi}{3}\frac{c}{v_g}k\frac{\Delta(2b)}{f} \tag{6-31}$$

where $k \approx (1.0)$ MHz/0.001 in. For example, an error of 1° corresponding to a $\Delta(2b)$ of 0.0002 in. can easily be eliminated. In practice, all cavities were initially machined to a diameter nominally 0.0005 in. oversize. This assured that after allowing for machining tolerances, the correct tuning of all cavities could be achieved by external dimpling, as described above.

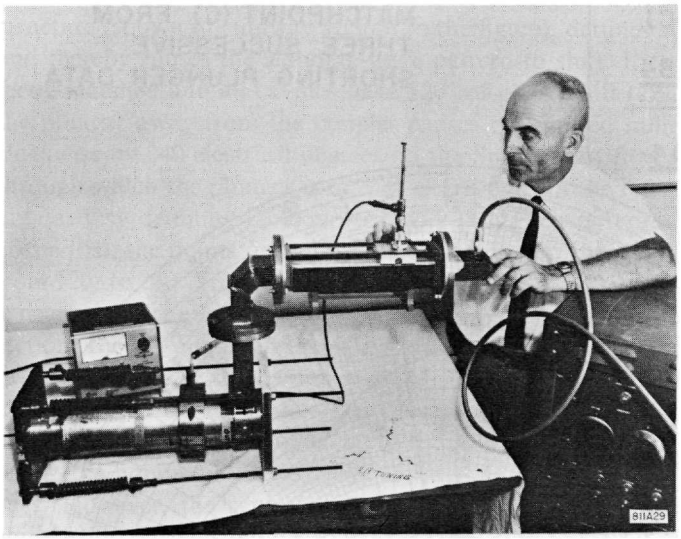

Figure 6-29 Experimental arrangement for tuning a short accelerator section, with illustration of tuning tool.

Because field lines can extend over a distance of three disks in the $2\pi/3$ mode configuration, tuning and matching strongly interact in the first cavities. It was pointed out[20] that this property can cause serious difficulties. If the coupler is not well matched, tuning the first cavities by bringing the points to the proper positions on the Smith chart can actually cause the following effect: successive cavities will have built-in cyclic phase errors $\Delta\phi_1$, $\Delta\phi_2$, $\Delta\phi_3$ which compensate for the reflection caused by the coupler. Since the VSWR for the nodal shift in the first cavities approaches infinity, the match point C is indistinguishable from the center O of the Smith chart, and the structure appears to be tuned and matched. In reality, a double or triple perodicity is built into the section, which causes passband splitting. It was predicted[20] that the split would occur at approximately the $\pi/2$ frequency for a $2\pi/3$ section. Precautions can be taken to avoid this possible ambiguity. One remedy consists of using a resistive plunger which even in the first cavities allows the position of the match point C to be identified. Another technique is to measure the phase of the wave reflected from the coupler and the adjacent (No. 1) cavity (assuming the dimensions of the latter cavity to be correct). By placing the tuning plunger alternately in cavities 1 and 2, the required condition of 120° phase shift per cavity may be approached iteratively by dimpling the coupler cavity and filing the coupling iris. In practice, this result was achieved by separately prematching the couplers with a perfect three-cavity assembly before final brazing of the section. A particular technique to prematch the coupler without a perfect three-cavity assembly has also been worked out[21] for particular use with a structure operating in the $2\pi/3$ mode.

In this technique it is necessary to know the frequency at which each cavity has $\pi/2$ phase shift. This method is useful in preventing any incorrect matching which could cause the incorrect tuning mentioned above.

A few additional remarks should be made:

1. The matching and tuning operation must be performed in a carefully temperature-controlled dry room. Sections should be allowed to stabilize thermally for several hours. Preferably, the tuning operation should be done with the section filled with dry air.

2. The detuning plunger should be light and clean in order to prevent damage or contamination of the disk edges. Notches should be provided so that the plunger always rests in the same relative position, or dwell point, around which small motions do not disturb the null. When tuning a constant-gradient section, where the $2a$ dimension changes as a function of length, the largest possible plunger compatible with the smallest $2a$ dimension should be used. It was verified that, in this manner, the dwell condition can be achieved in all cavities.

3. In the $2\pi/3$ mode it was found that moving the plunger by less than a full cavity away from the coupler causes the null on the slotted line to move toward the generator by one-half the phase shift introduced. This surprising effect is attributable to the manner in which the plunger detunes the cavity and not to any actual phase reversal. When the plunger finally moves into the dwell point in the next cavity, the null appears in the correct place.

4. Contrary to the early Mark III sections, the SLAC sections are provided with output couplers and loads to prevent a reflected wave from appearing at the klystron amplifiers. These couplers had to be tuned in the same manner as the input couplers, by switching over the whole experimental setup to the output coupler.

5. When an experimental section has been matched and tuned, three final RF checks are advisable: (1) The global match can be checked with a continuously movable short in the rectangular waveguide beyond the output coupler.[11] This measurement involves observing the image of two intersecting diameters on the Smith chart, transformed through the complete section including the two couplers. This image of the "iconocenter" must fall at the center of the chart. (2) The global match can be checked with a matched load at the output or input ends. (3) The attenuation can be measured globally for the entire section by direct substitution techniques, or for a part of the section by measuring the change in reflection coefficient as a function of plunger position.

Finally, it is often of interest to obtain a complete traveling-wave field plot for the entire accelerator section. This plot can be obtained by drawing a small metallic or dielectric needle along the axis of a disk-loaded waveguide structure which is excited at one end by a signal generator and matched at the other end with a load. The relative field amplitude is obtained by measuring either the reflection coefficient caused by the reflected wave from the bead, or the phase shift across the section caused by the forward-scattered wave from

the bead. The phase of the field can be measured by noting the phase of the reflection coefficient of the reflected wave.

It is interesting to note that if one wants to recheck the relative amplitude of the fundamental space harmonic ($a_0^2/\sum a_n^2$) by this method, both electric field amplitude and phase are needed, as shown by the derivation below. The total field is given by the expression

$$E_z(z, t) = \sum_{n=-\infty}^{n=+\infty} a_n(r) \exp[i(\omega t - \beta_n z)] \tag{6-32}$$

where β_n is the phase constant associated with the nth space harmonic. Integrating over the length of one cavity, one obtains

$$a_n = \frac{1}{d} \int_{-d/2}^{+d/2} E_z(z) \exp(j\beta_n z)\, dz \tag{6-33}$$

Notice, however, that E_z in this expression is a complex quantity of the form $|E_z(z)|e^{-j\theta(z)}$, where the plots of $|E_z(z)|$ and $\theta(z)$ are given by the perturbation measurements. Choosing the origin in the middle of a cavity and observing symmetry, it is then possible to obtain a_n and hence $a_0^2/\sum a_n^2$ by evaluating the integral

$$a_n = \frac{2}{d} \int_0^{d/2} |E_z(z)| \cos\,[\beta_n z - \theta(z)]\, dz \tag{6-34}$$

Generally, it is sufficient to calculate only three or four terms to obtain 1% accuracy.

It is also interesting to note why the traveling-wave measurement requires knowledge of both θ and $E_z(z)$ whereas the standing-wave measurement described above can be made with $E_c(z)$ alone. The reason is that in the cavity measurement, there are two waves traveling in opposite directions:

$$\begin{aligned} E_c(z, t) &= \sum_{n=-\infty}^{n=+\infty} a_n \exp[j(\omega t - \beta_n z)] + a_n \exp[j(\omega t + \beta_n z)] \\ &= \sum_{-\infty}^{+\infty} 2a_n \cos \beta_n z\; e^{(j\omega t)} \end{aligned} \tag{6-35}$$

Hence, a_n is given by

$$a_n = \frac{2}{\lambda} \int_0^{\lambda/2} E_c(z) \cos \beta_n z\, dz \tag{6-36}$$

where the quantity $E_c(z)$ is either positive or negative but contains no phase.

Dimensional correction made on the prototype section (RPB)

Final modifications in the dimensions of the disk apertures $2a$ (and accompanying changes in the cavity diameters $2b$) were made using data from completed 10-ft sections.[22] The technique consisted of comparing the

measured field variation and attenuation in a section with the field variation and attenuation required for a constant-gradient structure, taking into account the effect of beam loading. The original objective had been to arrive at a constant gradient with 10% beam loading. It was found, however, that this required too small a beam aperture. A minimum disk aperture of 0.750 in. was set, with the resulting structure having a constant gradient at about 5% loading.

For specified values of attenuation, fractional beam loading, and input power, and with known average shunt impedance of the structure, the ideal attenuation along the structure is given[23] by

$$A_n = \frac{1}{2}\frac{1}{(P_0/(\delta P)_{Tn}) - n}\left\{\frac{r_n i^2}{2(\delta P)_{Tn}} + 1 - \left[\left(\frac{r_n i^2}{2(\delta P)_{Tn}}\right)^2 + \frac{r_n i^2}{(\delta P)_{Tn}}\right]^{1/2}\right\} \quad (6\text{-}37)$$

where

A_n = loss due to dissipation in nth cavity (nepers)
P_0 = specified input power
$(\delta P)_{Tn}$ = power lost to beam and circuit in nth cavity
r_n = shunt impedance of nth cavity (assumed constant)
i = average beam current during pulse

Additionally, the average beam current during the pulse and the power lost to the beam and the circuit are obtained[24] from

$$i = (\text{fractional beam loading}) \cdot \left\{2\frac{(P_0 \sum_{n=0}^{N-1} r_n)^{1/2}(1 - e^{-2\tau})^{1/2}}{\sum_{n=0}^{N-1} r_n[1 - 2\tau e^{-2\tau}/(1 - e^{-2\tau})]}\right\} \quad (6\text{-}38)$$

and

$$(\delta P)_{Tn} = (\delta P)_{Bn} + \frac{(\delta P)_{Bn}^2}{i^2 r_n} \quad (6\text{-}39)$$

where $(\delta P)_{Bn}$, the energy absorbed by the beam in the nth cavity, is

$$(\delta P)_{Bn} = \frac{i}{N}\left\{\left(P_0 \sum_{n=0}^{N-1} r_n\right)^{1/2}(1 - e^{-2\tau})^{1/2} - \tfrac{1}{2} i \sum_{n=0}^{N-1} r_n\left(1 - \frac{2\tau e^{-2\tau}}{1 - e^{-2\tau}}\right)\right\} \quad (6\text{-}40)$$

Here τ is the total attenuation through the structure (nepers) without beam loading, and N equals total number of cavities in structure.

The power dissipated in the circuit is given by the term

$$\frac{(\delta P)_{Bn}^2}{i^2 r_n} \quad (6\text{-}41)$$

The desired values of circuit attentuation as represented by the A_n obtained from Eq. (6-37) were compared with values of A_n obtained from measurements of the relative field strength along the accelerator section and its

total attenuation. These measured values (denoted by primes) were obtained using

$$A_n' = A_0\left(\frac{E_n}{E_0}\right)^2 \exp\left(2\sum_{n=0}^{N-1} A_n'\right) \tag{6-42}$$

where E_n/E_0 is the relative strength in the nth cavity, and A_0, the loss in nepers in the first cavity due to RF dissipation, was determined, for use here, from the total attenuation measurement and data from the relative field strength plot. It is given by

$$A_0 = \frac{1 - e^{-2\tau}}{2\sum_{n=0}^{N-1}(E_n/E_0)^2} \tag{6-43}$$

The differences between the measured and required values of A_n in conjunction with group velocity measurements were used to obtain corrections for aperture diameter:

$$\Delta(2a)_n = \frac{(v_g/c)_n'[(A_n'/A_n) - 1]}{\partial(v_g/c)/\partial(2a)|_n} \tag{6-44}$$

Since changes in the disk aperture affect the phase velocity, they had to be compensated by corresponding changes in cylinder diameter ($2b$) using the relation

$$\Delta(2b) = \Delta(2a)\frac{\partial f/\partial(2a)}{\partial f/\partial(2b)} \tag{6-45}$$

The curves of $2a$ and $2b$ given in Fig. 6-22 for the thick disk case actually include the corrections made in accordance with the procedure just described. The numerical values for $2a$ and $2b$ are given in Table 6-6. These dimensions are predicated upon machining the copper disks and cylinders with the temperature of the cutting oil held at 65°F. The resulting temperature of the parts being machined was 69.7°F. Operation of the finished structure at a temperature of 113°F then results in a phase velocity in the structure equal to the velocity of light at a frequency of 2856 MHz.

The Coupler asymmetry problem and the "baba-abab" waveguide configuration (GAL)

The configuration of the waveguides feeding the accelerator, as illustrated in Fig. 5-17, was chosen as the best possible remedy to the problem of coupler asymmetry described in this section. This configuration follows the so-called baba-abab pattern, in which, looking downstream, an "a"-type waveguide feed comes from the left and a "b"-type feed comes from the right. Successive 40-ft girders alternate between the baba and the abab periodicity. How this fairly complicated configuration was arrived at is explained below.

In any normal accelerator cavity, the field configuration has cylindrical symmetry. However, the coupler cavity with its matching iris aperture is an

Table 6-6 Dimensions of constant-gradient accelerator section[a,b]

Cavity	*2b (in.)*	*2a (in.)*	*Cavity*	*2b (in.)*	*2a (in.)*	*Cavity*	*2b (in.)*	*2a (in.)*
Input coupler	3.0416[c]	0.7517[d]						
			29	3.2662	0.9631	58	3.2438	0.8713
1	3.2859	1.0323	30	3.2655	0.9603	59	3.2429	0.8677
2	3.2853	1.0300	31	3.2648	0.9575	60	3.2421	0.8640
3	3.2846	1.0277	32	3.2641	0.9547	61	3.2413	0.8603
4	3.2839	1.0254	33	3.2633	0.9518	62	3.2404	0.8565
5	3.2832	1.0231	34	3.2626	0.9489	63	3.2395	0.8527
6	3.2825	1.0207	35	3.2619	0.9460	64	3.2387	0.8488
7	3.2817	1.0183	36	3.2612	0.9431	65	3.2378	0.8449
8	3.2810	1.0159	37	3.2604	0.9401	66	3.2369	0.8409
9	3.2802	1.0135	38	3.2597	0.9371	67	3.2360	0.8369
10	3.2794	1.0111	39	3.2589	0.9341	68	3.2351	0.8329
11	3.2786	1.0087	40	3.2582	0.9310	69	3.2342	0.8288
12	3.2779	1.0063	41	3.2574	0.9279	70	3.2333	0.8246
13	3.2772	1.0039	42	3.2566	0.9248	71	3.2324	0.8204
14	3.2766	1.0015	43	3.2558	0.9217	72	3.2315	0.8161
15	3.2759	0.9991	44	3.2550	0.9185	73	3.2306	0.8117
16	3.2752	0.9967	45	3.2542	0.9153	74	3.2297	0.8072
17	3.2745	0.9943	46	3.2534	0.9121	75	3.2288	0.8027
18	3.2738	0.9918	47	3.2527	0.9089	76	3.2280	0.7981
19	3.2731	0.9893	48	3.2519	0.9056	77	3.2271	0.7934
20	3.2724	0.9868	49	3.2511	0.9023	78	3.2262	0.7886
21	3.2717	0.9843	50	3.2503	0.8990	79	3.2253	0.7836
22	3.2711	0.9817	51	3.2495	0.8956	80	3.2243	0.7786
23	3.2704	0.9791	52	3.2487	0.8922	81	3.2233	0.7735
24	3.2697	0.9765	53	3.2479	0.8888	82	3.2223	0.7682
25	3.2690	0.9739	54	3.2471	0.8854	83	3.2213	0.7628
26	3.2683	0.9712	55	3.2463	0.8819	84	3.2202	0.7573
27	3.2676	0.9685	56	3.2454	0.8784	Output coupler	3.1310[c]	0.7517
28	3.2669	0.9658	57	3.2446	0.8749	86		0.7517

[a] $2\pi/3$ mode, $\tau = 0.57$, $\rho = 0.1215$ in., $t = 0.2300$ in.

[b] Numbering convention: cavity numbers increase in the direction of beam travel; the dimension $2a$ opposite each cavity number is the diameter of the aperture in the up-beam disk of that cavity.

[c] The center for boring the half-wall of the input coupler cavity opposite the input waveguide has been displaced 0.1550 in. in a direction away from the waveguide. The purpose of this displacement is to compensate for the opening in the wall which allows power to flow into the cavity from the waveguide. The symmetry of the fields in the coupler cavity is thus approximately restored. The corresponding displacement for the output cavity is 0.0800 in.

[d] Beam entrance aperture into coupler.

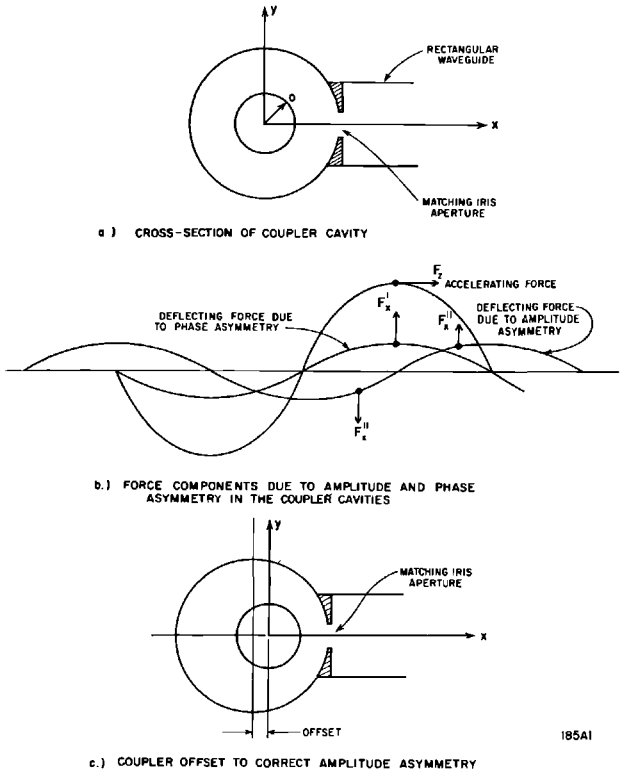

Figure 6-30 The coupler asymmetry problem.

exception. It had been known for a number of years that the longitudinal electric field in this cavity is slightly asymmetrical. Referring to Fig. 6-30a, E_z is somewhat larger on the right side, i.e., close to the iris, than on the left side. It had also been understood[25,26] that this transverse gradient of $|E_z|$ is equivalent to a magnetic field B_y which subjects the electrons to a Lorentz force F_x.

A subsequent examination of the E_z field by means of microwave perturbation measurements revealed that there were both amplitude and phase asymmetries in the transverse plane of the coupler. These measurements consisted of plotting both the amplitude and the phase of a wave reflected by a small longitudinal bead as a function of bead position in the coupler cavity. For an uncorrected cavity as shown in Fig. 6-30a, the amplitude asymmetry was of the order of 10% and the phase shift was of the order of 1.5° over the beam aperture.

To understand the effect of these asymmetries on the beam, let the spatial variation of E_z be of the form

$$E_z = \left[E_{z,0} + \frac{\Delta E}{2a}x\right] \exp\left[j\left(\frac{\Delta\phi}{2a}\right)x\right] \tag{6-46}$$

where ΔE and $\Delta\phi$ are the amplitude and phase variations in the x-direction over the aperture diameter $2a$ averaged from 0 to d, the cavity length. Then, to first order,

$$\frac{\partial E_z}{\partial x} = j\frac{\Delta\phi}{2a}E_{z,0}\exp\left[j\left(\frac{\Delta\phi}{2a}\right)x\right] + \frac{\Delta E}{2a}\exp\left[j\left(\frac{\Delta\phi}{2a}\right)x\right] \tag{6-47}$$

From Maxwell's equations, B_y and, hence, the Lorentz force F_x are both in time quadrature with $\partial E_z/\partial x$. Referring to Fig. 6-30b, the deflecting force F_x', caused by the phase asymmetry and proportional to $(\Delta\phi/2a)E_{z,0}$, is in phase with the accelerating force F_z; it produces a net deflection on a bunch traveling on the crest of the wave. On the other hand, the force F_x'', caused by the amplitude asymmetry and proportional to $(1/2a)(\Delta E/E_{z,0})E_{z,0}$, is in quadrature with the accelerating force F_z; its effect, as shown in an exaggerated form in Fig. 6-30b, is to spread transversely a bunch traveling on the accelerating wave crest. In practice, both of these effects occur simultaneously and are undesirable.

Using simple electrodynamics, it can be shown that the transverse momentum δp_x imparted to an electron traveling at an angle θ with respect to the accelerating wave crest through a coupler cavity of length d is given by

$$\delta p_x = \frac{eE_{z,0}\lambda d}{4\pi ac}\left[\Delta\phi\cos\theta + \frac{\Delta E}{E_{z,0}}\sin\theta\right] \tag{6-48}$$

This formula is also given in slightly different form in Eq. (7-107).

It was shown[26] that unless $\Delta E/E$ could be kept smaller than 0.1% and $\Delta\phi$ less than 0.06°, serious difficulties might arise in steering the beam over the 2-mile length. In particular, steering of multiple beams of different energies through accelerator sections which are powered for one beam (and hence cause a deflection) and unpowered for another (thus causing no deflection) would have been extremely difficult and probably impossible without pulsed steering magnets. To remedy these difficulties, several measures were taken.

1. Offsetting the coupler cavity as shown in Fig. 6-30c almost completely compensated for the amplitude asymmetry. The value of the offset was found through successive approximations using microwave perturbation measurements; for the input cavity it is 0.155 in. and for the output cavity, 0.080 in. Within the accuracy of the measurements, the value of $\Delta E/E$ was thereby reduced to 0.1% or less.

2. Attempts to compensate for the phase asymmetry inside the coupler cavity did not meet with a simple solution. Experiments which intentionally used slightly misaligned cavities were not successful in reducing $\Delta\phi$. The only practical solution appeared to be a symmetrically fed coupler cavity with two irises. However, such a solution would have been expensive and fairly impractical since it would have required an additional power splitter.

The baba-abab waveguide configuration shown in Fig. 5-17 is actually a practical version of the double iris coupler where the symmetrical feeding is

done on successive sections. Of all the alternative configurations, the abba-abba or baab-baab periodicities would have been the simplest because they would have re-established a parallel and axial beam over a 40-ft length. In practice, because of waveguide flange interferences, these configurations could not be adopted, and the baba-abab periodicity was chosen. Its only disadvantage is that over a 40-ft length, a beam entering on axis and parallel to it emerges parallel to the axis but with a net transverse displacement. The next 40-ft length produces the reverse effect and brings the beam back on axis. Hence this periodicity would require that klystrons be turned on and off in pairs so that over an 80-ft length the beam always remains on axis. In practice, this measure is never used. The effect is only serious at low energy in the first two or three sectors of the machine.[28] When a klystron must be turned off, the resulting steering effect is compensated by the dc magnetic steering dipoles available in the drift sections.

3. Although it was not possible to compensate for the phase asymmetry, its effect was reduced by causing the output coupler of a section to cancel part of the deflection created by the input coupler. Because the phase shift $\Delta\phi$ appears to be in the direction of power flow, this reduction in net deflection was obtained by having the input and output waveguide feeds on the same side. This remedy did not achieve total cancellation because the values of $(\Delta\phi/2a)_{\text{in}}$ and $(\Delta\phi/2a)_{\text{out}}$ differ by 30 to 40% in the constant-gradient structure.

6-3 Fabrication, assembly, and installation

Fabrication (ALE)

A number of techniques of fabricating disk-loaded waveguide capable of meeting the close tolerances necessary to obtain the correct phase and group velocities were explored at Stanford. Of the many methods considered, only three were ever used to construct accelerator sections, namely, shrinking, electroforming, and brazing. The shrinking method[2] was used at Stanford to construct the original 300-ft, 1-GeV accelerator (Mark III), but it was considered unsatisfactory for the SLAC machine when compared to the other two techniques.

Extensive work with electroforming and brazing demonstrated that satisfactory disk-loaded waveguide sections could be made by either of these techniques. The specification for maximum phase shift excursions at any point along the axis of a 10-ft section was set to $\pm 2.5°$. This corresponds to a mechanical tolerance of ± 0.00005 in. for $2b$; $+0.0002$ and -0.0000 in. for $2a$; ± 0.001 in. for d; ± 0.0002 in. for t; and ± 0.0005 in. for ρ (see Fig. 6-2). It is evident from these tolerances that special techniques had to be utilized if they were to be achieved economically.

The most exacting of the tolerances was the ± 0.00005 in. required for

the $2b$ dimension. The first step in meeting this requirement consisted of machining the parts that went into the assembly to a tolerance of $+0.0002$ and -0.0000 in. It was not sufficient simply to air-condition the room in which these parts were made; it was also essential that a temperature-controlled cutting solution be flowed over the parts during the machining operation. Hence, these parts were machined in an air-conditioned room and with a coolant oil, controlled within 0.25°C. After the assembly was completed, the equivalent of the 0.00005-in. tolerance was achieved by making slight deformations in the wall of each cavity as discussed briefly earlier in this chapter and described further below. This procedure was feasible with either the brazing or the electroforming methods of fabrication.

Satisfactory sections were obtained with both the electroforming and brazing techniques. However, extensive studies indicated that brazing was the preferable way of fabricating the 10,000 ft of disk-loaded waveguide. The decision to use the brazing technique was based primarily on the higher degree of flexibility inherent in this method; it required only a few hours to complete a brazed assembly, whereas it took 9 days to complete an electroformed assembly. However, it is significant to note that for the large-scale production required at SLAC, the cost of the electroforming technique was estimated to be the same as the cost of the brazing technique within the accuracy of the estimates. For the sake of completeness, descriptions of both fabrication techniques are included below.

Figure 6-31 shows an exploded view of the parts used for electroforming, together with a completed piece of disk-loaded waveguide made by this process. The first step in the electroforming method of fabrication was the assembly of a 10-ft array consisting of the copper disks and aluminum spacers shown in the figure. After the parts were assembled in a V-block, a mandrel was inserted through the holes to hold the assembly together. The assembly

Figure 6-31 Exploded view of parts assembled for the electroforming process.

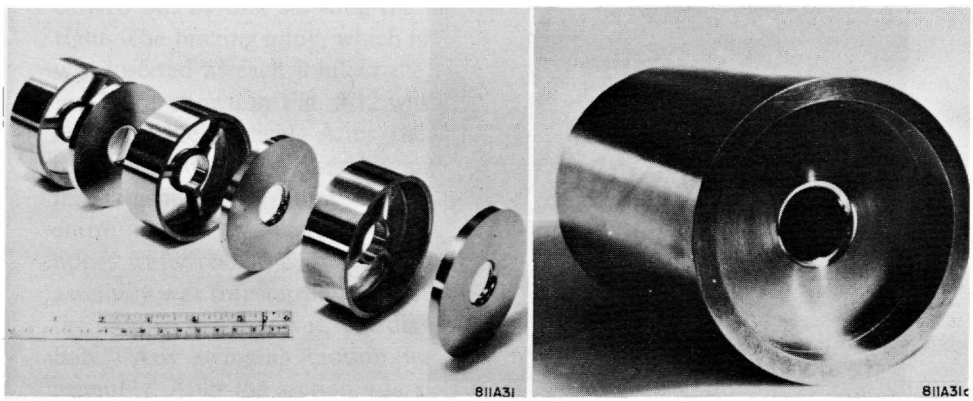

work was carried out under water to assure that the hydrostatic pressure was equalized, hence reducing the probability of solution leakage. After assembly, the array was chemically cleaned and processed, and a thickness of $\frac{3}{8}$ in. of copper was electroformed over it. Figure 6-32 shows the completed assembly in a copper sulfate electroforming bath. During this procedure, the mandrel was held horizontally with the assembly half-submerged in the solution. While plating, the assembly was rotated at approximately 30 rev/min. An agate burnisher was made to ride back and forth, continuously smoothing the surface of the plated copper. After the outer wall had been electroformed, the aluminum spacers were removed by etching in a sodium hydroxide solution. This procedure yielded an all-copper disk-loaded waveguide fabricated to very close dimensions. A comparison of the crystalline structure of copper electroformed by this technique with that of OFHC copper (oxygen-free high conductivity copper) produced by the usual, mill fabricating procedure showed that the metallurgical properties were very similar. Electroformed copper as it came from the bath had a surface finish of 6 μin. Nine days were required to deposit the $\frac{3}{8}$-in. wall thickness. Electroforming was used to produce a number of experimental 10-ft sections which exhibited excellent operating characteristics.

The study of various brazing techniques led to the development of a new type of furnace. The essential features of this furnace were a moving ring burner fired by an oxygen–hydrogen flame and a water-cooled chamber containing a reducing atmosphere in which the section was cooled. The essential

Figure 6-32 Assembly being electroformed.

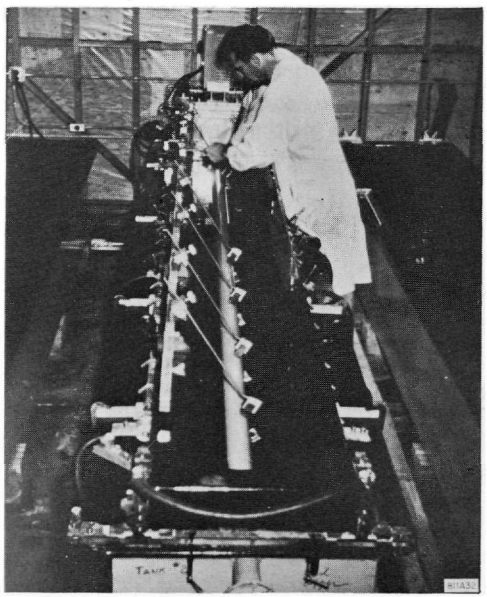

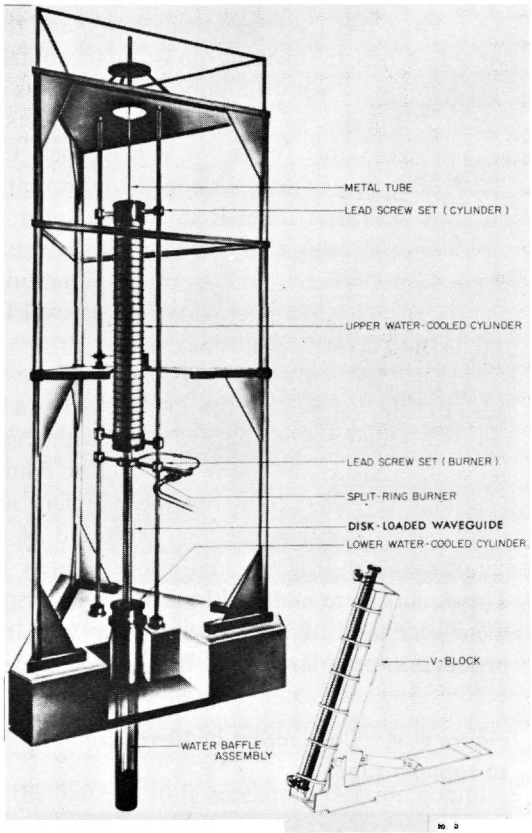

Figure 6-33 Schematic view of flame furnace.

features of the flame furnace are illustrated in Fig. 6-33 which shows a 10-ft section nearing the completion of the brazing cycle. The procedure was carried out by first stacking the parts in the V-block which is shown at the right. The brazing alloy, which is a silver–copper eutectic melting at 783°C, was inserted at each joint in the form of thin washers. The stacking of the unit parts shown in Fig. 5-12 was carried out while the V-block was at a 75° angle to the vertical. After the stacking was completed, a mandrel was inserted through the assembly and the end was clamped by a spring-loaded mechanism. The V-block was then tilted to the vertical position, and the entire assembly was moved into the furnace by means of a jib crane. The upper water-cooled cylinder was held in the fully raised position, while the assembly was transferred to the furnace and hooked onto a metal tube which then served to support it. The disk-loaded section then hung as a free "plumb bob." Any swinging motion was damped by means of the water baffle assembly. After the section was suspended, the split ring burner was closed

around the disk-loaded waveguide. The burner was then raised to the uppermost end of the disk-loaded waveguide and the oxygen–hydrogen burner was ignited. When the melting point of the brazing alloy was reached, the ring burner together with the upper cylinder was caused to move down the 10-ft section by means of the two lead screw sets. One lead screw set drove the cylinder, the other drove the ring burner. Oxidation of the interior of the disk-loaded waveguide section was prevented by flowing a reducing gas through the metal tube. Reducing gas also flowed into the upper cylinder, providing a reducing atmosphere for the exterior of the section. A period of 25 to 30 min was required from the initiation of the heating cycle to its completion. The section was ready for removal from the furnace $2\frac{1}{2}$ hours after the heating cycle was finished.

Figure 6-34 shows the connection of the 10-ft assembly to its supporting tube and the "nose" plate which served as a closure for the cylinder containing the reducing atmosphere in which the assembly was cooled. Figure 6-35 shows the furnace in operation with the flame on.

Input and output waveguide couplers were made up as separate subassemblies. Each subassembly consisted of the input or output waveguide coupler, the end flange, and approximately 8 in. of disk-loaded waveguide. These units were matched in advance as described earlier in this chapter and then were used in the stacking of a complete 10-ft section. Actually, once production on a large scale had started, the coupler parts were machined so

Figure 6-34 Connection of 10-ft assembly to support tube.

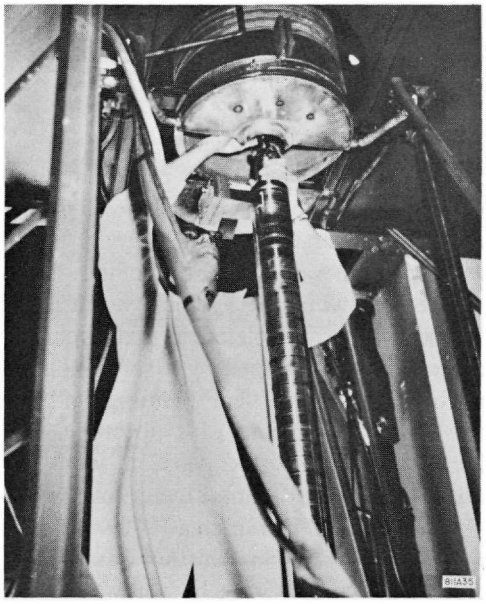

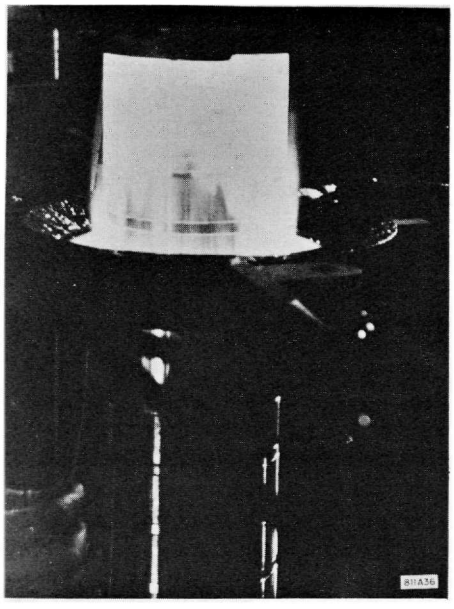

Figure 6-35 Furnace showing ring burner in operation.

accurately that no final matching was necessary to meet the maximum specified VSWR of 1.05.

Figure 5-13 shows a view of the finished 10-ft accelerator section complete with the water-cooling tubes which were attached by brazing in a separate furnace.

The maximum allowable phase tolerance per cavity of $\pm 2.5°$ was achieved by a tuning operation which consisted of indenting the walls of each cavity with four small dimples located at 90° about the axis. Figure 6-36 shows an overall view of the special tuning machine which was designed to tune the 10-ft accelerator sections while they were evacuated and at operating temperature. During the tuning procedure, the temperature was controlled to $\pm 0.1°F$. The inside diameters of the cylinders comprising the cavity walls were machined oversize, leaving approximately a 10° phase margin in each cavity for tuning.

The tuning apparatus consisted of the mechanism shown in Fig. 6-37 and a microwave bridge system[27] shown in block diagram form in Fig. 6-38. The bridge system consisted of a commercially available phase measuring unit which compared the signal reflected by a calibrated reference branch with that of a test branch containing the accelerator section. The unit utilized a double side-band suppressed-carrier technique. This technique was selected over other possible methods because it provided the required accuracy of approximately 0.1° phase and was not sensitive to changes in attenuation of

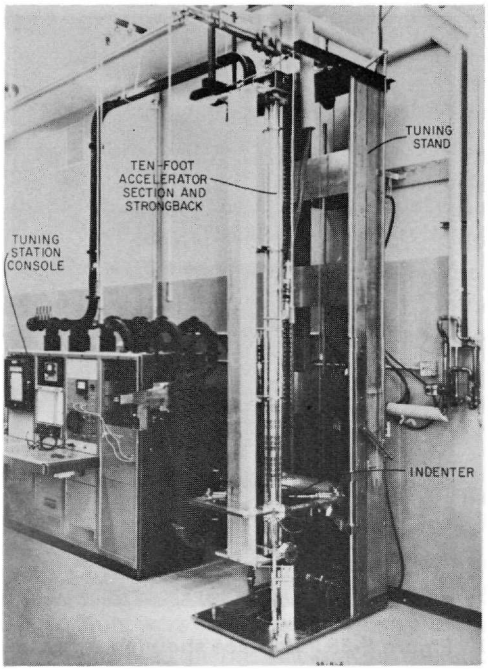

Figure 6-36 Overall view of the tuning machine.

the test signal with respect to the reference signal. Insensitivity to changes in attenuation was important because the amplitude of the wave reflected from the shorting plunger changed with the position of the plunger in the accelerator section. Furthermore, a unit was required that gave a direct phase readout so that the operator could monitor and control the amount of tuning required for each cavity. The mechanism by which the actual tuning was accomplished, illustrated in Fig. 6-37, worked in the following way: the movable carriage holding the indenters was indexed at the center of each cavity. Connected to the movable carriage was the expandable shorting plunger. The rod holding the plunger was coupled and indexed with the movable carriage by means of steel tapes. The indentation of the cavities was accomplished by means of four hydraulically driven cylinders which pushed the $\frac{3}{8}$-in. diameter indenters into the wall of the cavity. The plunger driving rod was made of Invar to insure dimensional stability in the location of the shorting plunger. Two O-ring seals allowed the rod to move into and out of the evacuated section.

The tuning of the section began with the installation of a 10-ft section as shown in Fig. 6-36. The reference arm of the bridge circuit was then calibrated by means of a reference standard which consisted of a precise, movable short with three calibrating positions corresponding to the three Smith chart

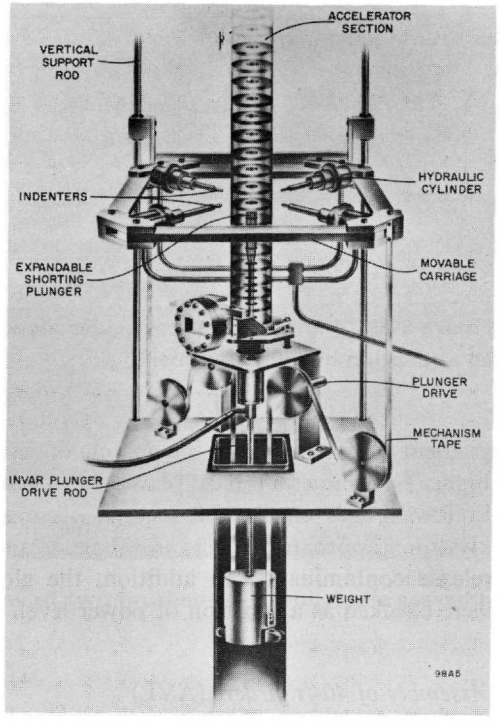

Figure 6-37 Tuning mechanism showing movable carriage and indenters.

branches for the $2\pi/3$ disk spacing of the accelerator structure. After calibration with the reference branch, the tuning of the individual cavities proceeded.

For quality control purposes, additional low-power measurements were made. Measurements were performed to check the phase of each cavity, the

Figure 6-38 Block diagram of the phase measuring system.

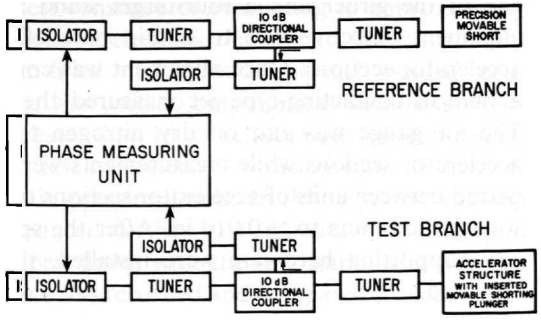

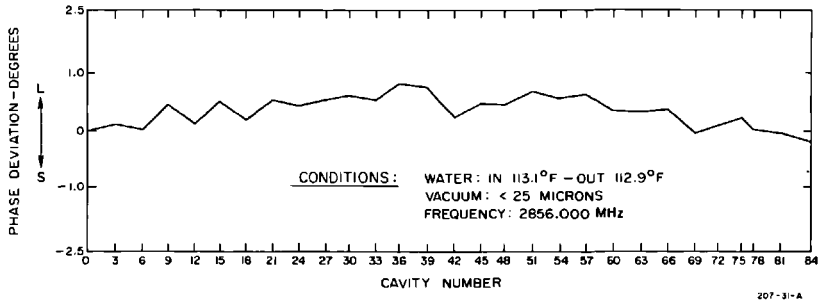

Figure 6-39 Plot of phase deviations along a 10-ft section after tuning, as a function of cavity number.

gradient along the axis, the match of each coupler, and the attenuation. Figure 6-39 shows a typical phase plot made during the quality control check. Following this check, the sections were subjected to high power from a klystron (approximately 15 MW peak and 15 kW average), primarily to release contaminants. In addition, the global phase shift and attenuation were checked as a function of power level.

Assembly of 40-ft girders (AVL)

The assembly and alignment of 40-ft lengths of accelerator were carried out in the shop (see Fig. 6-40) and these 40-ft segments were then installed in the accelerator housing. The accelerator sections were mounted on a 2-ft diameter, 40-ft long pipe which serves simultaneously as a vacuum envelope for the laser alignment system and as a support girder (see Chapter 22). Before placing the accelerator sections on the support girder, the girder was checked for vacuum leaks and the hardware for the laser alignment target was installed. The exterior of the sections was cleaned, one of the waveguide cap-off flanges was removed and a nitrogen purge line was connected, and the sections were then installed on the girder. The tooling provided for 6° of freedom, allowing the proper alignment of the sections on the girder. The alignment was achieved by means of a four-telescope alignment station at one end of the girder and a four-target stand at the opposite end. The initial alignment objective was to obtain parallelism of the mating faces of the accelerator sections. Once alignment was complete, a special air gauge using a built-in contacting-type jet measured the parallelism within ± 0.0001 in. The air gauge was run on dry nitrogen to prevent contamination of the accelerator sections while measurements were being made. Spacer rings were placed between ends of accelerator sections to adjust the distance between the waveguide inputs to ± 0.010 in. After the spacer rings and all the mounting and supporting hardware were installed, the special support tooling was removed.

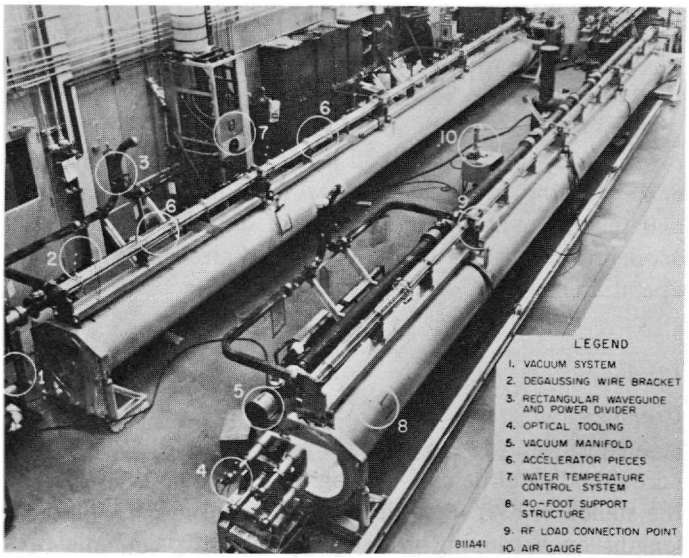

Figure 6-40 View of two finished 40-ft modules in assembly shop.

The vacuum manifold was then installed, and the accelerator sections were precisely aligned using the optical tooling holes in the 10-ft accelerator section supports. The alignment tolerance allowed only 0.001 in. displacement of any accelerator section relative to its adjoining section and a maximum of 0.005 in. total straightness error. Twist had to be avoided since the welded joints between 10-ft sections are extremely stiff in torsion, and once the weld was made, the error could not be removed. After alignment, the joints between 10-ft sections were welded using argon cover gas and nitrogen backing gas.

At this point, the rectangular waveguide S-assemblies (see Chapter 11) were installed, bolted to the waveguide input, and welded to the vacuum manifold. Then RF loads were added.

Following this installation, the assembly was vacuum tested. Two vacuum tests were performed. The first test consisted of evacuating to approximately 10^{-1} torr, connecting a mass spectrometer leak detector to the system, and leak checking by placing helium-filled enclosures about each welded, end-bolted joint. A fine helium probe was used to pinpoint leak locations where necessary. Any detected leaks (greater than 10^{-10} cc/sec) were repaired before proceeding. The second vacuum test consisted of measurements of pressure and time required to attain certain pressure levels. In this test, the vacuum was roughed down to 1 torr, reduced further to 10^{-4} torr with the liquid nitrogen thimble, and then pumped down with the ion pump. The time required to reach each pressure point was recorded and compared to a standard.

The vacuum envelope had to attain 3×10^{-7} torr in less than 8 hours to be acceptable. Upon completion of the vacuum checks, the accelerator was pressurized to 2 psig with dry nitrogen and pinched off.

Several parallel operations were carried out simultaneously with the vacuum tests. These included the connection of all plumbing to the accelerator sections, waveguides, and loads, and installation of magnetic shielding, demagnetizing, and degaussing wires. Final alignment was then carried out, and the girder assembly was loaded onto a transporter for the trip to the accelerator housing. A more detailed description of the girder assembly operation can be found in Reference 29.

Installation (AVL)

Completed girder assemblies were transported from the assembly area to the accelerator housing on a special trailer. The trailer length was adjustable to accommodate girders of varying lengths (from the 9-ft drift section girder to the standard 40-ft long girder) by placing girder support frames of various lengths on a running gear equipped with pneumatic tires. The maximum acceleration of the girder assembly in transit was specified to be 0.3 *g*. An accelerometer was mounted on the girders during transport and the dynamic loading was recorded. The maximum allowable loading of 0.3 *g* was not exceeded and nearly all girder assemblies were subjected to a dynamic loading of less than 0.2 *g*.

The girder assemblies were transported on the special trailer over the road to the west portal of the accelerator housing and up the aisle in the accelerator housing to their approximate final location. Two air-film supported pallets were then placed under the girder support frame and the running gear was removed. The air-film supported pallets allowed the entire assembly to be slipped sideways from the aisle into the beam line and adjusted to the correct position. Figure 6-41 shows a girder being moved from the aisle side of the accelerator housing into the beam line position. The girder was raised to the correct elevation by means of jacks built into the pallets. The girder weight was then transferred to the floor jacks, and the girder support frame and air-film supported pallets were removed.

After the girders were set in place and roughly aligned, connections were made to the penetration waveguides. The vacuum manifold was welded to the vacuum finger and to the vacuum manifold on the adjoining girders, and the beam line intergirder bellows were welded. When all the girders within a sector were installed and the vacuum system was completed as described above, the entire sector was evacuated. After evacuation and connection of the water-cooling lines to the accelerator sections and waveguide, the waveguide was phase tuned (see Chapter 11).

Subsequently, the downbeam end of each girder was accurately positioned with respect to the upbeam end of the following girder in the cross-joint alignment process. This process is described in Chapter 22. Upon completion,

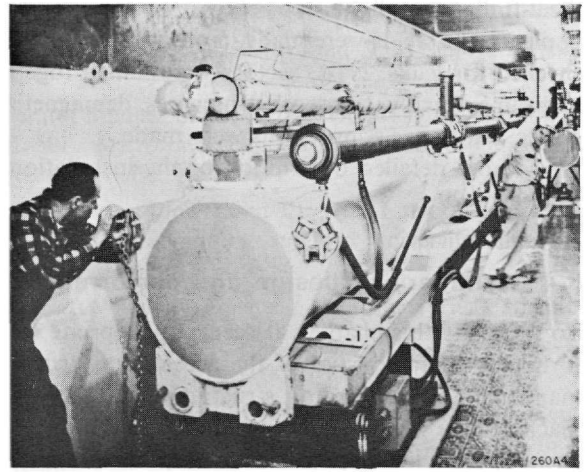

Figure 6-41 Positioning of a 40-ft girder in the accelerator housing.

Table 6-7 Final design and performance of the SLAC accelerator structure

No. of standard 10-ft sections	940
No. of 7-ft sections	12
No. of cavities in each 10-ft section	84 + 2 couplers
Distance between inputs of two consecutive sections on a girder	29λ or 87 cavities
Phase shift per cavity	$2\pi/3$
Operating frequency (nominal)	2856 MHz
Measured frequency for maximum electron energy at 113°F operating temperature	2855.980 MHz
Accelerator wall temperature increase with average input power	0.42°C/kW
Frequency change necessary to track temperature change	100 kHz/2°C
Normalized group velocity range, v_g/c	0.0204–0.0065
Range of shunt impedance r_0 (for fundamental space harmonic) in 10-ft section obtained by microwave measurements	53–60 megohms/meter
Attenuation parameter τ in 10-ft section	0.57
Filling time t_F	0.83 μsec
Efficiency[a] $K = V/P^{1/2}$, where V is in MeV per 10-ft section and P is in MW into the section	
Theoretical, based on $\bar{r}_0 = 56.5$ megohms/meter	10.75 MeV/(MW)$^{1/2}$
Experimental (average over entire accelerator)	10.65 MeV/(MW)$^{1/2}$
Beam loading derivative	35 MeV/mA

[a] When the output power from a single klystron supplying four 10-ft sections is referred to, the respective numbers are ≈20.2 and 20. The rectangular waveguide loss is ≈0.54 ± 0.1 dB.

the 2-ft diameter, light pipe bellows were inserted between girders and welded in place. The welds were made in one sector at a time and the sector was then checked for leaks. Next, sectors were joined together and checked for leaks in groups. Finally, the degaussing wires, demagnetizing wires, phase reference cables, and other connections were made.

A more detailed description of the installation process can be found in Reference 29.

6-4 Summary of design and performance (GAL)

To conclude this chapter, it seems appropriate to summarize the main performance characteristics of the accelerator structure. Of course, the performance of the accelerator structure cannot be divorced from that of the machine as a whole, and hence, many of the operational results have already been reported in Chapter 5. In retrospect, it can be said that, so far, the accelerator structure has lived up to all the expectations and specifications for which it was designed. It has failed only in one respect in that the cumulative, multisection-type of beam breakup was not foreseen in advance. This problem continues to be under intensive investigation as this book is being written and a detailed up-to-date discussion can be found in Chapter 7. The final design and performance data of the accelerator structure are summarized in Table 6-7.

Acknowledgments

The authors would like to thank those members of the Stanford Linear Accelerator Center staff who have contributed to the work reported here. In particular, they wish to acknowledge the contributions of O. Altenmueller, W. J. Gallagher, B. Kendall, A. Kirshbaum, C. Kruse, J. Abraham, L. Cain, R. Chapton, M. Heinz, D. Jeong, F. Patton, J. A. Pope, C. Rasmussen, D. Robertson, D. Rogers, K. Skarpaas, H. Soderstrom, and B. Stillman.

References

1 E. L. Ginzton, W. W. Hansen, and W. R. Kennedy, *Rev. Sci. Instr.* **19**, 89 (1948).

2 M. Chodorow *et al.*, *Rev. Sci. Instr.* **26**, 134 (1955).

3 R. B. Neal, "Theory of the Constant Gradient Linear Electron Accelerator," Rept. No. ML-513, Microwave Laboratory, Stanford University, Stanford, California (1958); and "Comparison of the Constant Gradient and Uniform Accelerator Structures," Rept. No. M-259, Stanford Linear Accelerator Center, Stanford University, Stanford, California (1961).

4 J. E. Leiss and R. A. Schrack, "Transient and Beam Loading Phenomena in Linear Electron Accelerators," Internal Report, Natl. Bur. Standards, Washington, D.C. (October 30, 1962).

5 M. G. Kelliher and R. Beadle, *Nature* **187**, 1099 (1960).

6 M. C. Crowley-Milling, T. R. Jarvis, C. W. Miller, and G. Saxon, *Nature* **191**, 483 (1961).

7 "Linear Electron Accelerator Studies; Status Rept. 1 October to 31 December, 1958," Rept. No. ML-581, Microwave Laboratory, Stanford University, Stanford, California (February 1959).

8 P. B. Wilson, "A Study of Beam-Blow up-in Electron Linacs," Rept. No. HEPL-297, High Energy Physics Laboratory, Stanford University, Stanford, California (June 1963).

9 R. Kingsland, Hughes Aircraft Company, Fullerton, California (private communication).

10 E. L. Ginzton, *Microwave Measurement*, McGraw-Hill, New York, 1957.

11 W. J. Gallagher, "Measurement Techniques for Periodic Structures," Rept. No. M-205, Stanford Linear Accelerator Center, Stanford University, Stanford, California (November 1960).

12 P. N. Robson, "Fourier Series Representations of Dispersion Curves for Circular Corrugated Waveguide Used in Traveling-Wave Linear Accelerators," Rept. No. 5105, Metropolitan-Vickers Electrical Company, Ltd., Manchester, England (1956).

13 W. R. Ayers, E. L. Chu, and W. J. Gallagher, "Measurements of Interaction Impedance in Periodic Circuits," Rept. No. ML-403, Microwave Laboratory, Stanford University, Stanford, California (June 1957).

14 "Linear Electron Accelerator Studies and Proposed Two-Mile Accelerator Project; (combined) Status Report, 1 October to 31 December 1960," Rept. No. M-246, Stanford Linear Accelerator Center, Stanford University, Stanford, California (January 1961).

15 K. B. Mallory, "A source of error in the use of slope detection for perturbation measurements," *Inst. Radio Engrs. Trans. Microwave Theory Tech.*, **10**, 146 (1962).

16 Renée Hirel, "Space-Harmonic Content of the $2\pi/3$ Accelerator Structure," Rept. No. M-270, Stanford Linear Accelerator Center, Stanford University, Stanford, California (1961).

17 G. A. Deschamps, *J. Appl. Phys.* **24**, 1046 (1953).

18 Kenneth Brandt Mallory, "A comparison of the predicted and observed performances of a billion-volt electron accelerator," Ph.D. Thesis, Stanford University, Stanford, California (1955), p. 68 *et seq.*

19 R. Belbéoch, "Problèmes posés par l'adaption du coupleur d'entrée d'une structure en guide chargé par des iris," Rept. No. LAL-13, Laboratoire de L'accélerateur Linéaire, Orsay, France (1961).

20 R. Kyhl (private communication).

21 E. Westbrook, "Microwave Impedance Matching of Feed Waveguides to the Disk-Loaded Accelerator Structure Operating in the $2\pi/3$ Mode," Tech. Note SLAC-TN-63-103, Stanford Linear Accelerator Center, Stanford University, Stanford, California (December 1963).

22 R. Borghi and D. Jeong, "Gradient Corrections for the SLAC Accelerating Structure," Tech. Note SLAC-TN-63-60, Stanford Linear Accelerator Center, Stanford University, Stanford, California (1963).

23 R. B. Neal, "Theory of the Constant Gradient Linear Electron Accelerator," Rept. No. ML-513, Microwave Laboratory, Stanford University, Stanford, California (1958), p. 4, Eq. (3.6).

24 R. B. Neal, "Comparison of the Constant Gradient and Uniform Accelerator Structures," Rept. No. M-259, Stanford Linear Accelerator Center, Stanford University, Stanford, California (1961), p. 5, Eq. (7).

25 R. H. Helm, "A Note on Coupler Asymmetries in Long Linear Accelerators," Rept. No. M-167, Stanford Linear Accelerator Center, Stanford University, Stanford, California (1960).

26 R. H. Helm, "Effects of Stray Magnetic Fields and RF Coupler Asymmetry in the Two-Mile Accelerator with Sector Focusing," Rept. No. SLAC-20, Stanford Linear Accelerator Center, Stanford University, Stanford, California (October 1963).

27 R. Borghi, F. Patton, and M. Heinz, Phase velocity adjustment of the SLAC accelerating structure (private communication).

28 SLAC Staff, "Consolidation of Results of Preliminary Beam Tests with Sectors 1 and 2," Rept. No. SLAC-50, Stanford Linear Accelerator Center, Stanford University, Stanford, California (1965).

29 A. Lisin, "Girder Assembly and Installation," Tech. Note SLAC TN-67-17, Stanford Linear Accelerator Center, Stanford University, Stanford, California (May 1967).